Chapter 2
Collisionless Reconnection and Electron Demagnetization

J.D. Scudder

Abstract Observable, dimensionless properties of the electron diffusion region of collisionless magnetic reconnection are motivated and benchmarked in two and three dimensional Particle In Cell (PIC) simulations as appropriate for measurements with present state of the art spacecraft. The dimensionless quantities of this paper invariably trace their origin to breaking the magnetization of the thermal electrons. Several observable proxies are also motivated for the rate of frozen flux violation and a parameter Λ_Φ that when greater than unity is associated with close proximity to the analogue of the saddle point region of 2D reconnection usually called the electron diffusion region. Analogous regions to the electron diffusion region of 2D reconnection with $\Lambda_\Phi > 1$ have been identified in 3D simulations. 10–20 disjoint diffusion regions are identified and the geometrical patterns of their locations illustrated. First examples of associations between local observables based on electron demagnetization and global diagnostics (like squashing) are also presented. A by product of these studies is the development of a single spacecraft determinations of gradient scales in the plasma.

Keywords 3D reconnection • Collisionless reconnection • Demagnetization observables • Diffusion region • Electron demagnetization • Reconnection site

2.1 Introduction

Magnetic reconnection is thought to be made possible by the existence of a "diffusion" region where "physics beyond Alfvén's ideal MHD" facilitates a steep, but smooth, transition between asymptotically sheared magnetic fields. Such a transition effects an interconnection of the previously unlinked, but sheared, magnetic field lines enabling a reorganization of their topology; after reconnection previously skew magnetic field lines pierce the plane of the current sheet. Before reconnection particle populations on either side of the current sheet could not interpenetrate; after

J.D. Scudder (✉)
Department of Physics and Astronomy, University of Iowa, Iowa City, IA, USA
e-mail: jack-scudder@uiowa.edu

W. Gonzalez, E. Parker (eds.), *Magnetic Reconnection*, Astrophysics and Space Science Library 427, DOI 10.1007/978-3-319-26432-5_2

reconnection previously separated plasmas can mix with the advent of components of **B** normal to the current sheet. Prior to steepening such a sheared current channel might be viewed as a classical *tangential discontinuity, (TD)*. As a non-propagating limit of a slow wave, whose normal has become perpendicular to the local magnetic field (Burlaga 1995), this layer is in pressure equilibrium. In nature the current channel of a TD usually occurs with thermal ion gyro radius scales. Theoretically this channel can form a Vlasov equilibrium with scales as small as the electron gyro-scale (Burlaga and Lemaire 1978), although they are usually unstable. Collisionless reconnection can arise in the unstable disruption of such layers (and with the evolution of other initial configurations) when the current channel has narrowed to widths of the order of the electron inertial lengths in the plasma which are the skin depth, $d_e \equiv c/\omega_{pe}$ and the thermal gyro radius, $\rho_e \equiv w_{\perp,e}/\Omega_{ce}$. The electron plasma and cyclotron frequencies are defined by $\omega_{pe}^2 \equiv 4\pi ne^2/m$ and $\Omega_{ce} \equiv eB/mc$, respectively. The j'th species' average rms thermal speed transverse to the magnetic field is denoted $w_{\perp,j} \equiv \sqrt{2kT_{\perp,j}/M_j}$, where M_j is the particles mass and c is the vacuum speed of light. This particle's transverse thermal speed and cyclotron frequency determine its thermal gyro radius $\rho_j = w_{\perp,j}/\Omega_{cj}$.

Alfvén's ideal MHD is an approximation frequently made to simplify the description of plasmas *when they only possess very long spatial scales* $L >> \rho_i$ *and possess very weak time dependence compared to the cyclotron frequencies*. As useful as the ideal MHD approximation can be, it does *not* apply everywhere in a plasma; the physics of magnetic reconnection is only describable by foregoing the simplifications of Alfvén's keen early insight.

While precise mathematical definitions of reconnection have been proposed in 3D geometries, such relationships are usually non-local conditions that are even difficult to verify within simulations, let alone testable with the most advanced, but relatively local, experiments flown on small spacecraft armadas. Even in 2D geometries the mathematical conditions are difficult to experimentally parse, since they define reconnection to be *possible* when not equal conditions of the form $\mathbf{Y} \neq 0$ are fulfilled, where Y is some relationship between flow, electric and magnetic fields. Care should be taken to note that such conditions may be *necessary* for reconnection to ensue, but their satisfaction is generally not *sufficient* to identify reconnection as having been witnessed.

In this chapter the discussion focuses on likely *observable* properties that the inner "diffusion" layer of the reconnection channel might have, while showing that these properties are restatements of, or are rare proxies for the more stringent theoretical definitions. In some circumstances we will argue that necessary conditions of the form $\mathbf{Y} \neq 0$ will need to be strengthened to $|\mathbf{Y}| > a > 0$, with a non-zero value of a before the necessary condition becomes selective enough to identify layers that are actually undergoing magnetic reconnection (cf. Sect. 2.4.1ff).

A commonly cited condition for characterizing magnetic reconnection involves testing for conversion of electromagnetic energy into plasma energy, $J_\parallel E_\parallel > 0$, where the parallel subscript denotes the component along the local magnetic field direction: $G_\parallel \equiv \mathbf{G} \cdot \hat{\mathbf{b}}$. To date no direct measurements of these quantities have ever been made together at the same location in space. Both observables are difficult

measurements; recent progress on $E_\parallel$ detection has been made with long wire booms, but detection of electron inertial scaled $J_\parallel$ layers is exceedingly difficult. Their determination is outside the scope of curlometer approaches, Dunlop and Balogh (2005), with spacecraft flotilla since collision avoidance of the spacecraft keeps the multi-point observations separated on scales broad compared to that of the expected current channels. Direct detection of the current density from particle measurements are impacted by the different time resolutions of electron and ion sensors needed for adequate counting rates and the need to determine 3D number fluxes $n_k\mathbf{V}_k$ for all charged species in the plasma, including those sequential (and, therefore, time aliased) estimates made for different ion species: $\mathbf{J(t)} = \Sigma_k Z_k n_k(t)|e|\mathbf{V}_k(t)$. Even on the recently launched Magnetospheric Multi-Scale (MMS) mission the fastest time scale for determining all necessary contributions from particles for $\mathbf{J}$ is acquired across a total collection time of 10s (South West Research Institute 2010; Fuselier, 2015, private communication). For typical relative motions of the spacecraft such time resolution is still beyond that required at the noon magnetopause to measure $J_\parallel E_\parallel$ directly. Using measured profiles from the magnetometer requires intricate and usually unknown knowledge of the world line of the observations of the profile to *estimate the current density* $\mathbf{J}$. Typically available measurements constrain the integrated change of the current ΔI much more accurately than the current density, that is theoretically required. Accordingly, the desired identification of the reconnection locales must explore other more accessible observables. Unfortunately there are a large number of conceptually critical quantities that are not directly observable. Accordingly, a somewhat indirect approach is required to establish the locales and properties of reconnection layers in space.

Our approach requires the certification of observables that could be made from spacecraft and a description of the electrodynamics that satisfies the theoretician that magnetic reconnection produced the signatures being inventoried. Clearly this argument would be tautological if made using *in situ* data. This chapter profits from using 2 and 3D Particle In Cell (PIC) simulations of reconnection layers which allow internal diagnostics not available to the spacecraft borne observer, which can be used to assure the theoretician that the layers inventoried are signatures of magnetic reconnection. PIC codes can also sidestep the important and troublesome closure problems present in other truncated fluid descriptions of space plasmas such as occur with various forms of MHD. At the same time a subset of PIC output quantities can determine the state of the art spacecraft observables as signatures of the layer. As will become clear in this chapter this inner current channel is distinguished by its effect on electrons, the smallest gyro radii particles in the plasma. Because PIC codes follow the equations of motion of individual electron and ion proxies, the fidelity of the aggregate dynamical picture they allow is clearer than models of reconnection that describe this physics from the reduced fluid pictures of MHD or extended MHD.

We will find it profitable to reframe desirable theoretical quantities from the vantage point of the electrons in the form of the *Generalized Ohm's Law* (Rossi and Olbert 1970). This relationship replaces assumptions like $\mathbf{E} = \eta\mathbf{J}$ with those more appropriate for a wide range of collisionalities, including the troublesome

collisionless regimes commonly occurring in space plasmas. Importantly, the PIC approach allows all of the terms present in this law to be evaluated. The key to detection of reconnection sites will be through electron specific observables and the electric field $\mathbf{R}_e$ reckoned in the rest frame of the bulk of the electrons, which moves in the laboratory frame with velocity $\mathbf{U}_e$. This electric field recurs so often that it is given its own symbol, $\mathbf{R}_e \equiv \mathbf{E} + \mathbf{U_e} \times \mathbf{B}/c$, and its own name, the *Non-Ideal Electric Field*, since its size is above and beyond the common place *Unipolar, or Ideal Electric Field*, caused by motion of the electron fluid relative to the magnetic field: $\mathbf{E}_{ideal} = -\mathbf{U}_e \times \mathbf{B}/c$. This reduced electric field occurs naturally as two of the terms in the Generalized Ohm's Law.

In Alfvén's ideal MHD this unipolar ideal electric field is essentially the *same* as seen in the center of mass frame of the plasma or in any species frame of reference, since by assumption these are weak current regimes and all these frames of reference are the same. For the electron rest frame observer we review below that the apparent time dependence of the magnetic flux is controlled by the $\nabla \times \mathbf{R}_e$. This approach greatly clarifies the physics that is often attempted with extended MHD language; as the current densities increase and the plasma scales reach below the ion inertial lengths this approach provides much needed clarity for the processes that can take place, including reconnection, whether in the collisional or collisionless regimes.

In this chapter we develop an observational program for this inner layer of the current channel that we will refer to below as the *Electron Diffusion Region (EDR)*. We will show that this layer's special character is that it has gradient scales, L, smaller than the thermal electron's gyro radius, ρ_e; this circumstance contradicts that supposed when deriving MHD, where scale lengths are assumed to be much larger than any particle gyro radius ($L >> \rho_i > \rho_e$); thus, it is not surprising that non-MHD phenomena may be caused by such a layer. Observationally layers with these scales are also extremely rare in astrophysics, not being a required part of wave normal modes or discontinuities. Accordingly, *defensible* detections of electron inertial scaled current channels are to be highly prized when seeking to identify sites of collisionless magnetic reconnection. At the same time we address the difficulty of measure spatial scales in moving media, resolving this problem by showing that suitable dimensionless ratios like ρ_e/L are direct observables with modern state of the art plasma observations.

In MHD regimes the gradient scales are assumed to be longer than the gyro radii of either electrons or ions so that the magnetic field strength appears to the individual particle in the plasma to be slowly varying in space and time. These weak variations permit one to predict from classical mechanics that the magnetic moments $\mu_j = w^2_{\perp,j}/B$ of the particles will be adiabatically conserved, with the moment calculated from the particle's circular current formed by its motion transverse to the field. μ_e conservation for the electrons implies that the magnetic flux linked by the gyro orbit is conserved, or loosely, electrons can "follow" a magnetic line of force as it gradually changes strength, direction or becomes slowly time dependent.

With the smallest mass in the plasma, the electron's inability to "follow" a magnetic line of force is much more noteworthy *and rare* than the circumstances where ion's cannot follow the same tube of force. Magnetic moment disruption for

ions is considerably more common because the spatial scale of disruptive gradients need only approach the ion gyro radius for this purpose which occurs in nearly every MHD discontinuity, like *tangential discontinuities (TD), rotational discontinuities (RD), fast and slow shocks, and their wave antecedents*.

Unlike the MHD regime, the electron diffusion region with $L < \rho_e$ is a place where the electrons are said to be *demagnetized*, because the weak gradient premises of this adiabaticity are not realized there. Vasyliunas identified that this demagnetization of electrons was a *necessary* property of symmetric collisionless reconnection layer in 2D (Vasyliunas 1975).

A common misconception is that μ_j conservation/violation occurring in the j'th particles can be ascertained by monitoring the constancy of a moment quantity $kT_{\perp j}/B$ possessing the same units as μ_j. It is easy to construct Vlasov solutions that conserve μ for every particle, but do not conserve the moment related quantity (Scudder et al. 1986). Thus, detection of variability of $kT_{\perp j}/B$ *need not* imply demagnetization of the j'th species.

The signature of the violation of μ_e conservation is that the electron probability distribution in the proper frame, $f_e(\mathbf{w})$, depends *intrinsically* on all three polar variables $|\mathbf{w}|, \theta_w, \phi_w$, where $\mathbf{w} \equiv \mathbf{v} - \mathbf{U_e}$ is the electron velocity relative to the laboratory frame electron bulk velocity, $\mathbf{U}_e$. Making observations that can discern this behavior requires simultaneous sampling of all octants of velocity space, which is possible with the present state of the art of plasma instrumentation; however, measurements that have used spacecraft rotation to build up the gyro-phase distribution of the 3-D velocity distribution are invariably aliased against detecting these signatures. In addition defensible determinations of $\mathbf{U}_e$ in the presence of UV, photo-electrons, spacecraft charging and the time aliasing of data acquisition is a necessary experimental prerequisite for experimental detection of these expected gyro phase dependences within the electron diffusion region.

In this chapter we extend Vasyliunas' original insight into 3D models of reconnection, demonstrating theoretically and with PIC simulations that this inner layer is characterized by demagnetized thermal electrons with observable consequences. While the circumstances of electron demagnetization are expected to be very rare in astrophysical plasmas, not all demagnetized layers are the electron diffusion region; demagnetization will also be shown to occur in other narrow current channels on the separatrices of the overall reconnection layer (where frozen flux violations are very much weaker). Nonetheless, this demagnetization, if perceptible, is a significant sieve for separating resolved two fluid current layers from electron inertial length scaled layers that are potentially reconnecting. *While demagnetization does not define the EDR layer alone, it represents an astrophysically rare, necessary, local, and observable kinetic property for a current layer to be a candidate layer where collisionless magnetic reconnection might be underway.*

Other theoretical considerations of *generalized* magnetic reconnection (GMR) have found it necessary to define its occurrence in 3D in terms of *global attributes* of the process. In this approach magnetic reconnection is defined by *non-local* tests about *the magnetic topology*. Often it is defined as occurring by finding *singular curves/loop integrals* that possess non-zero integrated $E_\parallel$, (Hesse et al. 2005).

Alternately, magnetic reconnection is said to require sheafs of field lines that are initially localized in close proximity, but undergo exponential separation, forming *quasi-separatrix layers*. Field lines that participate in such rapidly separating quasi-separatrix environments have flux tube cross sections that are flattened into highly elliptical cross sections, a global property made quantitative by non-locally determining their *squashing factors*, σ, Titov et al. (2002) and Demoulin et al. (1996). These considerations are amplified in Chap. 3 of this monograph (Priest 2016).

As theoretically useful as such concepts may be, these non-local properties are hard to verify using single spacecraft measurements, or even a flotilla of single spacecraft measurements such as those of Cluster or Magnetospheric Multi-Scale (MMS); they may not even be possible to discern except using global snapshots from 3D simulations. If these non-local criterion are critical for discerning reconnection in the 3D astrophysical context, there would appear to be insurmountable observational difficulties to provide *in situ* experimental closure with spacecraft data of sites where it occurs. A brief discussion of some initial attempts to connect local observables with these global concepts will be discussed in Section 2.9.3 of this chapter.

There is also the thorny issue of whether the enabling site of collisionless reconnection in 3D remains conceptually similar to the compact electron inertial scaled region suggested by the isolated "X" saddle point of the flux function that forms in simple 2D models. In 2D the *flux function* is the component of the vector potential orthogonal to the plane of allowed spatial variations. If this plane of variability is the x-y plane, the flux function $A_z(x, y, t)$ completely determines the variations of the magnetic field in the x-y plane (via the x and y components of $\mathbf{B} = \nabla \times \mathbf{A}$). In 3D analogous flux functions do not exist, making the global inventory of magnetic topology difficult. A very real possibility exists in 3D that reconnection sites might be spawned in some loose association by flux ropes enabled by other sites, with multiple ones coexisting in the same general pattern (Daughton et al. 2011). To observationally characterize how reconnection occurs in this likely situation would appear to require a program based on assaying physical properties of the layers encountered, not seeking to verify preconceived geometrical arrangements using 2D electron diffusion regions as the archetype. *We outline a procedure that appears to find the analogue of the electron diffusion region in 3D PIC simulations with the same methodology that correctly identifies the saddle point region of the 2D simulation where the flux function incontrovertibly has already established the locale of the EDR.*

The technical and mathematical conditions for reconnection in textbooks can be rather challenging to verify. Take for example "... reconnection occurs if there is an electric field, $\mathbf{E}$ along the *separator*, $\hat{\mathbf{S}}$", that is when $\mathbf{E} \cdot \hat{\mathbf{S}} \neq 0$. Other attempts to define locally the process of magnetic reconnection also end up specifying something else that is not zero. Examples are "... magnetic reconnection occurs whenever the *non-ideal electric field* $\mathbf{R}_e \neq 0$". Still others insist that magnetic reconnection occurs in the presence of quasi-separator curves delineated by flux

tube path integrals and $\int_B E_\parallel ds \neq 0$. Recently a theoretician suggested reconnection could be identified by finding the regions where $n_e - n_i \neq 0$. The required *frozen flux violation* for magnetic reconnection takes the form $\nabla \times \mathbf{R}_e \neq 0$. Vasyliunas' arguments (Vasyliunas 1975) suggested the site of 2D symmetric collisionless reconnection to be a place where the thermal electrons were not magnetized, which is yet another *not equal to zero* condition: $\partial f(\mathbf{w})/\partial \phi_w \neq 0$. *Even if all the quantities were measurable for these conditions, they do not suggest how large a violation of zero would confirm the occurrence of magnetic reconnection in the data.*

All the conditions in the previous paragraph are of the form $Y \neq 0$, making Y a *thresholdless variable, usually having dimensions*. Such conditions are experimentally difficult to test. The noise of measurement, ΔY, can always satisfy a thresholdless condition. Surely that is not enough to identify a site of magnetic reconnection. Far better would be to couch the theory in terms of *thresholded and dimensionless* conditions, that establish a minimum $\sigma_Y \neq 0$ for verification that a process, effect or condition had been witnessed. Whenever $Y/\sigma_Y > 1$ and $\Delta Y/\sigma_Y << 1$ one has a non-trivial measure of signal to noise for the decision. Lastly, but most important, the dimensionless test must be framed in terms of what is *observable* with the current state of the art instrumentation; thus, nothing involving delineating separators or measuring space charge densities is in this category at present. For example, in space, there is no local observable Y that determines the rate at which magnetic flux is being dissipated or the violation of the electron's magnetic moment, yet one still wishes to identify layers where this and related properties have transpired to advance and test the present theoretical understanding of reconnection.

This chapter is about reorganizing what is presently known about collisionless magnetic reconnection to produce observable, thresholded, dimensionless tests specific to identifying the electron diffusion region; an observable test is one that can be conducted with presently available state of the art plasma and fields measurements deployed on available spacecraft. As will be clear when our list is formulated, such tests will represent sieves of increasing probability that the electron diffusion region has been transited.

A short tour of frequently cited observables for reconnection that are used in the literature is provided in Fig. 2.1, Scudder (2015); those labeled "P-" are jump conditions from conservations for layers that Pass a mass flux. As indicated by the multiple situations (columns) with "X's" in them, these tests are not specific to the properties of *only* reconnection sites. The A* test is also tailored to identifying torsional transitions, such as Alfvén waves, or *rotational discontinuities (RD's)*, that transmit a mass flux while also shearing the magnetic field between their asymptotic states. Any locally planar disturbance that propagates through the plasma satisfies the "P-" or "A*" property.

While these tests may be necessary to screen discontinuities or waves that pass mass flux as some reconnection models require, they are for such common conditions in the plasma, by themselves they do not possess strong leverage for identifying the layer as a part of the process of magnetic reconnection. Even the frequently cited incidence of *"jetting"* or observations of flow acceleration are not

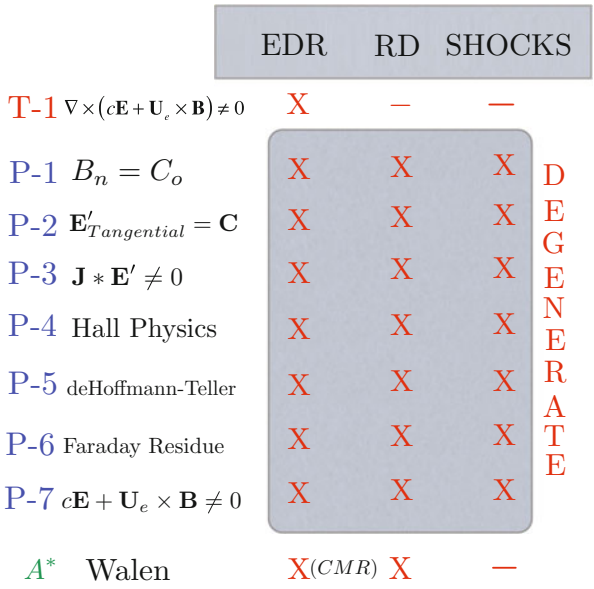

Fig. 2.1 Tests used for magnetic reconnection detection in space plasmas (Scudder 2015). P- are the flux passing test for planar layers (Paschmann and Daley 1998); A* is the Alfvénic or Walén tests used in the literature. The theoretical T−1 test from Faraday's law is discussed in this chapter, but has not been tested in space. Subscripts n and tangential refer to the local plane tangential to the current layer. Primed variables are observed in the rest frame of the current sheet. The deHoffmann-Teller frame test checks for the existence of a frame of reference outside the layer were changes of the fluid velocity and magnetic field are parallel. The Faraday Residue test attempts to identify a non-zero conserved normal component of B_n (Gauss' law) and conserved components of $\mathbf{E}\times\hat{\mathbf{n}}$, which from the $\nabla\mathbf{E} = 0$ implies the layer traversed has a *rest frame* where the transition can be viewed as time stationary. The Faraday residue test is usually performed with a flow proxy $\mathbf{E} = -\mathbf{U}\times\mathbf{B}/c$ and magnetic fields $\mathbf{B}$. The Faraday residue test is an alternate test for non-zero mass flux, best performed with electric and magnetic field observations. The X's in a given row denote the classes of layers where the test applies. When multiple X's are in a row, many different layers can pass such a test. $\mathbf{J}\cdot\mathbf{E}'\neq\mathbf{0}$ corresponds to energy exchanged with the electromagnetic field in the rest frame of the discontinuity, a process that occurs in most MHD transitions, whether involving reconnection or not. This quantity measures the work done by the layer in the rest frame of the layer and is generally partitioned between particles and fields; by contrast the Galilean invariant quantity $J_{\|}E_{\|}$ determines the net energy made available from the fields to the plasma, which if greater than zero reflects one of the hallmarks of magnetic reconnection: a shift of field energy into plasma energy

peculiar to reconnection, but are the hallmark of tangential accelerations that are *the property of Alfvénic structures wherever they are found*. Thus to our point, *the identification of the reconnection site cannot primarily rely on the detection of the P- and A* signatures as a certification of the reconnection layer*. Performing multiple tests successfully in the P- list can not strengthen the experimental case that a reconnection layer has been transited, since any layer that passes a give P- test should pass all of them, if the data quality and calibration are adequate for the test.

2.2 Magnetic Reconnection

If steady 2D magnetic reconnection is described with spatial variations allowed in the x-y plane, a time independent *reconnection* electric field, E_z is required parallel to the current sheet implied by the abutting magnetic fields where $\mathbf{B_1} \cdot \mathbf{B_2} < 0$. In steady state a long way away from the current sheet E_z is determined by the ideal electric field of MHD: $E_z = -\hat{\mathbf{z}} \cdot \mathbf{U_e} \times \mathbf{B}/c$; in this asymptotic regime the plasma is idealized as essentially current and gradient free, as Alfvén's hypothesized, where $\mathbf{U} = \mathbf{U}_i = \mathbf{U}_e$, where $\mathbf{U}$ is the center of mass velocity.

Faraday's equation $\partial \mathbf{B}/\partial t = -c\nabla \times \mathbf{E}$ for the plasma has many different approximations where various terms are assumed important. In the frame where the electrons are at rest (moving with velocity $\mathbf{U}_e$ in the laboratory frame) the left hand side becomes a total derivative and $\mathbf{E}$ is transformed by Galilean effects to become

$$\left.\frac{D\mathbf{B}}{Dt}\right|_{\mathbf{U}_e} = -c\nabla \times \mathbf{R}_e, \tag{2.1}$$

where the total derivative in the frame moving with velocity $\mathbf{W}$ satisfies the operator identity $D/Dt|_{\mathbf{W}} = \partial/\partial t + \mathbf{W} \cdot \nabla$. This rate of change is controlled by the circulation of the *non-ideal electric field* $\mathbf{R}_e$ defined in three equivalent ways:

$$\mathbf{R}_e \equiv \mathbf{E} + \mathbf{U}_e \times \mathbf{B}/c, \quad (I) \tag{2.2}$$

and from the steady state electron momentum equation

$$\mathbf{R}_e = -\frac{1}{en_e}\Big[\nabla \cdot \mathbf{P}_e + \nabla \cdot (mn\mathbf{U}_e\mathbf{U}_e)\Big] + \eta\mathbf{J} + TF(\mathbf{q}_e), \quad (II) \tag{2.3}$$

where the *resistive electric field* $\eta\mathbf{J}$ is defined by

$$\eta\mathbf{J} = -en_e m\nu_{ei}(\mathbf{U}_e - \mathbf{U}_i), \tag{2.4}$$

ν_{ei} is the electron ion coulomb collision rate, and *TF* is emf associated with the thermal force, a friction between electrons and ions that is caused by the pear shaped (skewed) electron distributions that reflect the presence of heat flow (Braginskii 1965).

Finally, a form for $\mathbf{R}_e$ in terms of the *ion* flow velocity can avoid using the electron flow velocity at the expense of including the *Hall emf* in the last term:

$$\mathbf{R}_e \equiv \mathbf{E} + \frac{\mathbf{U}_i \times \mathbf{B}}{c} - \frac{\mathbf{J} \times \mathbf{B}}{nec}. \quad (III) \tag{2.5}$$

Form (III) is often used, but its equivalence to form (I) clearly establishes that the Hall emf is (1) not able to disrupt the magnetic field from being frozen to the *electron rest frame* and that (2) when the Hall emf's are suggested to be necessary

for *fast magnetic reconnection* to occur, their need could be viewed as arguments that *all* the freedom of a two fluid plasma must be permitted to get fast reconnection, including electron pressure gradients and the electron thermal force of version (II). Because the Hall emf is not an agent for disrupting frozen flux as reckoned by the electron rest frame observer, its occurrence in the so called *ion diffusion region*, where Hall electric and magnetic signatures are observed, is not really a signature of the frozen flux violation *for the electron rest frame observer*. Alternately, the evolution equation for magnetic field lines continues to exist throughout the two fluid ion diffusion region, because they are advected there by, and frozen into the rest frame of the electrons (cf. Appendix 2).

2.2.1 Frozen Flux Violation

Consider a comoving, closed, right handed, orientable path C, with outward vectorial area **A** along the local magnetic field direction, with differential normal $\hat{\mathbf{b}}dA$. Using Stokes theorem on Eq. (2.1) determines an equation for the rate of change of magnetic flux, Φ, penetrating **A** for the observer moving with the electron bulk speed $\mathbf{U}_e$ (Priest and Forbes 2000; Schindler 2000), viz:

$$\left.\frac{D\Phi}{Dt}\right|_{\mathbf{U}_e} = -c\oint_C \hat{\mathbf{b}}\cdot\mathbf{R}_e ds. \tag{2.6}$$

The time scale for this frozen flux change can be determined as

$$\nu_\Phi \equiv \tau_\Phi^{-1} = \left|\frac{Dln\Phi}{Dt}\right|_{\mathbf{U}_e}. \tag{2.7}$$

Similar expressions can be determined for departures from *line preservation* with rates for this process indicated by $\nu_\uparrow$ (Birn and Priest 2000; Scudder et al. 2015a).

When the RHS of Eq. (2.6) vanishes *Alfvén's Frozen Flux Theorem of Ideal MHD* is implied. If at time t the magnetic flux is "frozen", it means that the equation of motion for a magnetic field line (a) exists, (b) is locally the same as determined from the electron fluid velocity, and (c) in an increment *dt* that the field line's location may be predicted to have moved *transverse* to itself a distance $d\mathbf{s}(\mathbf{x}) = (\mathbf{U}(\mathbf{x})_e - (\mathbf{U}(\mathbf{x})_e\cdot\hat{\mathbf{b}}(\mathbf{x}))\hat{\mathbf{b}}(\mathbf{x}))dt$, and is well described by the $\mathbf{B}(\mathbf{x}+d\mathbf{s}(\mathbf{x}), dt)$. In this situation there is no lateral slippage between the magnetic tube of force and the local velocity of the electron fluid perpendicular to **B**. This theorem supposes $\nabla\times\mathbf{R}_e \equiv 0$; frequently revered as if it were a law of physics, the theorem loses its predictive power in those physical circumstances, like reconnection, where this precondition is no longer fulfilled. However, since the violations require gradients and a circulation of $\mathbf{R}_e$ the very long scale lengths of variation supposed by Alfvén weaken the possible size of this violation unless $\mathbf{R}_e$ simultaneously became large in such weak gradient regions. However, since $\mathbf{R}_e$ is a "left over" electric field above

and beyond the unipolar **E**, one is hard pressed to suggest a physical system with very large scales where $\mathbf{R}_e$ grows to keep its curl sizable. This is the content of Alfvén's argument when he introduced his frozen in approximation.

When the frozen flux theorem is violated the mental image of field lines being "carried" by the electron flow (in the above sense) is no longer strictly true. Here, too, there is the absence of a threshold: slippage between the electrons and **B** may occur, but be *innocuous*, while at other times the slippage is absolutely essential to the dynamics of the process. Innocuous slippage occurs in many places, since Alfvén's frozen flux theorem is an idealization, akin to the no friction assumptions that are common in first year mechanics problems. "Substantial" frozen flux violations accompany *magnetic topology change*, a process that would not be possible if the motion of magnetic field lines and the average cross field motion of the electrons were always mathematically the same.

2.2.2 "Broken" Field Lines

These considerations are also involved in reconciling the perplexing MHD description of magnetic reconnection as a "cutting and restitching" of magnetic curves. When decisive frozen flux violations occur the rearrangement *over time* of magnetic field lines is not predicted by the electron kinematic description (Schindler 2000; Birn and Priest 2000). Nonetheless, a spatial picture of the magnetic field can be deduced at any "freeze frame", but the *temporal evolution of their rearrangements* is richer than the simple kinematic picture of magnetic field lines as spaghetti advected by the electrons. In this sense the violation of Alfvén's frozen flux approximation reflects the hidden degrees of freedom that the Maxwell-Plasma system has that do not conform to a kinematic picture of the electrons advancing the location of tubes of force in the medium. These violations occur in locations with electron inertial scale spatial gradients far removed from the large scale systems Alfvén had in mind when suggesting the *frozen flux* simplification.

2.2.3 Regimes of Frozen Flux

The *frozen flux condition*

$$\nabla \times \mathbf{R}_e = 0 \tag{2.8}$$

can be satisfied in many ways. Deciding that Eq. (2.8) has been violated has proven to be a vexing problem for experimentalists with spacecraft time series data. Alfvén's *frozen in* condition, $\mathbf{R}_e = 0$, is the simplest condition that implies the *frozen flux* condition is true, but it clearly is not the only one. In the space literature the circumstances of violating the "frozen in condition" are commonly inverted

to suggest that such observations imply violations of the "frozen flux condition." Alfvén's frozen in condition is sufficient, but not necessary, for satisfying the frozen flux condition. Simple counterexamples where $R_e \neq 0$ and the flux remains frozen are $\mathbf{R}_e = \nabla\psi$ where ψ is a scalar function, or $\mathbf{R}_e = -\nabla P_e(n)/(en)$, where P_e is a scalar functional of n. For the theorist this implies that polytrope closures will not allow collisionless reconnection. By such examples, experimental detections of *large* values for $\mathbf{R}_e \neq 0$ have no *necessary* claim on being sites for frozen flux violation. Detection of significant $E_\parallel$ (Mozer 2005), which is clearly part of $\hat{\mathbf{b}} \cdot \mathbf{R}_e \neq 0$, are an inadequate basis for routinely identifying sites of frozen flux violation (Scudder et al. 2008). As seen from Eq. (2.6) Stokes loop integrals of $\hat{\mathbf{b}} \cdot \mathbf{R}_e$, rather than spot readings, are required to be non-zero to show violations of the frozen flux condition. To date such loop integrals have not been produced empirically.

2.3 Taxonomy of Non-ideal Effects

Clearly, violations of frozen flux are required for magnetic reconnection. Although such violations are *necessary* for magnetic reconnection, they are *not always sufficient* indicators of magnetic reconnection. Making decisions of this type will hinge on the time scales τ_Φ of the frozen flux violation [cf. Eq. (2.7)], since Alfvén's suggestion of *ideal MHD* is based on an assumed scale free medium with time scales for slippage assumed infinite; this idealization has frozen flux decaying at an excruciatingly slow time scale, that in first approximation is ignorable.

If magnetic reconnection is to be defined, including a necessary threshold of sufficient frozen flux violation, there must be a way to differentiate locales where magnetic reconnection is dynamically important from those with innocuous slippage that exist when $\mathbf{R}_e$ has finite curls, because the scale lengths of variation are longer than electron inertial scales but still not infinite. We set this as our focus in this chapter.

The theoretical study of magnetic reconnection requires retaining *some non-zero* $\mathbf{R}_e$ *that has a non-vanishing curl*. When $\mathbf{R}_e \neq 0$ is retained in the description of the system it is referred to as a description via *non-ideal MHD*. The separation of the effect of the *ideal* unipolar electric field seen by the observer at rest in the electron frame in the LHS of Eq. (2.6) makes it clear that the electric field contributions retained on the RHS in $\mathbf{R}_e$ are not necessarily retained for their numerical importance relative to the unipolar motional electric field, but are being retained for what processes they structurally enable in the time and space evolution of the magneto-fluid.

To avoid the complexity of the general form for $\mathbf{R}_e$, a considerable literature exists discussing resistive reconnection that explores what may be learned without treating $\mathbf{R}_e$ in its full quantitative form. Some modelers have argued that it does not matter what is used for $\mathbf{R}_e$, so long as it has a curl. Clearly that argument is not

without exceptions, since so called *fast reconnection* with rates near $0.1V_A$ were not recovered until $\mathbf{R}_e$ was modified to include so called *Hall effect terms* that allow two fluid electrodynamics in the current sheet, while spatially uniform resistive terms that treat the fluid as a single entity were ineffective for this purpose.

There is thus a two tiered approach: (1) the ideal processes are always addressed with the LHS of Eq. (2.6), and (2) *selected* forms of $\mathbf{R}_e$ that are retained on the RHS for analysis of possibly new effects. Frankly, some choices in the literature reflect avoiding the serious theoretical roadblocks to entertain more realistic treatments, although this is changing with the advent of full Particle in Cell *PIC* and some multi-fluid simulations that avoid most of these concerns, but contain challenges of their own.

2.3.1 Coulomb Collisional Regime

By far the simplest regime is the *collisional regime* where $\mathbf{R}_e$ is replaced by the *Ohmic emf*:

$$\mathbf{R}_e \simeq \eta \mathbf{J} = \frac{m\nu_{ei}(\mathbf{U}_i - \mathbf{U}_e)}{en_e}, \tag{2.9}$$

but neglecting the *thermal force*, $TF(q)$, which also scales with collision rate and the heat flux. The cgs resistivity is given by $\eta_{cgs} = m\nu_{ei}/(ne^2)$, where ν_{ei} is the electron ion coulomb collision rate. Since the collision rate is proportional to density, the non-constant properties of the resistivity involve its reduction as T_e increases according to the $T_e^{-3/2}$; this dependence can be important as the dissipation heats the electrons in the current sheet. Physically this heating is spatially dependent, but *usually* η is considered as uniform in space and constant in time when studying problems of this type.

The ohmic emf has a curl so that $-c\nabla \times \mathbf{R}_e = \mathscr{D}\nabla^2\mathbf{B}$, where the diffusivity $\mathscr{D}$ (assumed uniform in space and constant in time) is given by $\mathscr{D} = c^2\eta_{cgs}/(4\pi ne^2) = d_e^2\nu_{ei}$. In this resistive approximation Faraday's equation becomes a simple parabolic vector diffusion equation for $\mathbf{B}$ in the comoving frame of the electrons:

$$\tau_{ei}\frac{D\mathbf{B}}{Dt}\Big|_{\mathbf{U}_e} = d_e^2\nabla^2\mathbf{B}, \tag{2.10}$$

where $\tau_{ei}^{-1} = \nu_{ei}$ is the coulomb electron ion mean rate for momentum transfer. The form of Eq. (2.10) shows that the *natural length scale for coulomb resistive diffusion is the electron inertial length, d_e, but the time scale for this process is the time scale for electron-ion collisions*. The origin of the term *electron diffusion region (EDR)* is from this resistive MHD form of the reconnection problem, where the magnetic field profile actually satisfies a mathematical diffusion equation within the current channel. In present usage the EDR refers to the layer where the current is channeled,

regardless of the mathematical form of the equation(s) that determine the transition profile, even if they are not parabolic differential equations.

By neglecting the thermal force *and the T_e dependence of η* this modeling is not hampered by the other limitation of reduced theoretical models of magnetic reconnection: *closure*. Closure is the process that effects a truncation of the infinite number of moments of the kinetic equation for the plasma, that for example might suggest how heat flows when there are gradients in the temperature and density. Actually the neglect of the T_e dependence of η is partially to avoid the closure issues of how to advance the temperature without knowing *a priori* the form of the heat law.

Throughout almost all locales of the current sheet the *ideal* left hand side of Faraday's equation dominates the *non-ideal* right hand side, even in the resistive regime. The ratio of LHS to RHS is the *magnetic Reynolds number, R_m*, that in most astrophysical contexts generally exceeds 10^6; however, the tiny but non-zero non-ideal RHS enables structural changes (including changes in apparent connectedness of asymptotically disconnected lines of force) that the left hand side cannot, no matter how disparate their sizes may be.

2.3.2 *Collisionless Terms of* $\mathbf{R}_e$

The remaining terms of $\mathbf{R}_e$ are the possible *collisionless* causes for magnetic reconnection, since unlike η and *TF* they do not involve the binary collision rate ν_{ei}. These are

$$\mathbf{R}_e^{less} = -\frac{\nabla \cdot \mathbf{P}_e + \nabla \cdot (mn_e\mathbf{U}_e\mathbf{U}_e) + \frac{\partial mn_e\mathbf{U}_e}{\partial t})}{en_e} \tag{2.11}$$

In order, these terms are known as the *diamagnetic*, *dynamic* and *acceleration* terms, although as specific terms in the electron momentum equation they all are forces per unit charge density felt by the electron fluid in the plasma.

We show below that Vasyliunas' argument places the gradient scale of the *diamagnetic* term in the reconnection channels as having a scale $L \simeq \rho_e \equiv \beta_e^{1/2} d_e$ at least at the separator of symmetric 2D reconnection. In the literature arguments appear that the diamagnetic term can be ignored (closure phobia!) by only considering low $\beta_e << 1$; however, the natural progress of collisional and collisionless reconnection raises the electron temperature and weakens B so that the current channel actually occurs in a higher β_e than its value outside the current layer (cf. Fig. 2.9). The diamagnetic term starts to grow on the d_i scale, when the two fluid effects commence with ions and electrons taking different paths through the layer and the diamagnetic pressure forces compensate for the new $\mathbf{J} \times \mathbf{B}$ force that occurs in the one fluid description.

Vasyliunas' assay pertains to the inner electron diffusion region of a symmetric reconnection layer where the electrons are demagnetized. In terms of the electron thermal Mach number, $M_e \equiv U_e/w_{\perp,e}$, the dynamic pressure term is $O(M_e^2)$ times the diamagnetic term. While $M_e << 1$ in traditional MHD, as we develop below it is expected to be order unity within the current sheet. In steady state the acceleration term vanishes, but in dynamic phases it clearly can be the same order as the other terms. In the collisionless regime this term supports displacement current effects in the emf which generally occur with ω_{pe} time scales, that are also frequently ignored, appealing to MHD ordering. At times the anomalous resistance used in modeling is said to reflect effects from this acceleration term. Therefore, in the current sheet of magnetic reconnection the hierarchy of terms in $\mathbf{R}_e$ are (diamagnetic:dynamic) and are expected in the proportion $(1 : M_e^2)$, with the dynamic pressure terms possibly competitive with the diamagnetic terms near the saddle point, where as shown below $M_e \simeq 1$. The diamagnetic and dynamic terms can survive in steady state, while the acceleration term is usually ignored.

2.3.2.1 Scales of Electron Diffusion Region

If steady magnetic reconnection is to be possible one of first two terms in the RHS of Eq. (2.11) must produce an emf, E_z, out of the plane when 2D variations are allowed in the x-y plane. Enforcing this condition at the stagnation point (in 2D) of a symmetric reconnection layer shows that the divergence of the dynamic pressure is not available for this purpose, since it vanishes there in this limit $mn(\mathbf{U}_e \cdot \nabla)\mathbf{U}_e = 0$. The diamagnetic term's divergence of the electron pressure tensor must perform this role (Vasyliunas 1975).

Since in 2D the partial derivatives of the divergence act only in the x-y plane, the E_z component is possible via

$$\hat{\mathbf{z}} \cdot \nabla \cdot \mathbf{P}_e = \frac{\partial P_{e,xz}}{\partial x} + \frac{\partial P_{e,yz}}{\partial y}. \tag{2.12}$$

Assuming that the electrons remain magnetized implies (MacMahon 1965) that the form of $\mathbf{P}_e$ can be given by

$$P_{e,ij}^{gyro} = P_{e,\parallel} b_i b_j + P_{e,\perp}(\delta_{ij} - b_i b_j), \tag{2.13}$$

where $P_{e,k}$ are the three eigenvalues of the pressure tensor, two of which are equal and associated with eigenvectors perpendicular to $\mathbf{B}$. [In the isotropic pressure regime the eigenvectors have no preferred direction.] Components of unit vectors

along the magnetic field are denoted by $b_k = B_k/|\mathbf{B}|$ and δ_{ij} is the well known Kronecker delta. Equation (2.12) may now be evaluated as

$$\hat{\mathbf{z}} \cdot \nabla \cdot \mathbf{P}_e \simeq \hat{\mathbf{z}} \cdot \nabla \cdot \mathbf{P}_e^{gyro} = \mathscr{Q}_I + \mathscr{Q}_{II} + \mathscr{Q}_{III}, \tag{2.14}$$

where

$$\mathscr{Q}_I \equiv \frac{\partial(P_{e,\parallel} - P_{e,\perp})}{\partial x}[b_x]b_z + \frac{\partial(P_{e,\parallel} - P_{e,\perp}}{\partial y}[b_y]b_z \tag{2.15}$$

$$\mathscr{Q}_{II} \equiv (P_{e,\parallel} - P_{e,\perp})\Big[\frac{\partial b_x}{\partial x}\Big]b_z + (P_{e,\parallel} - P_{e,\perp})\Big[\frac{\partial b_y}{\partial y}\Big]b_z \tag{2.16}$$

$$\mathscr{Q}_{III} \equiv (P_{e,\parallel} - P_{e,\perp})bx\Big[\frac{\partial b_z}{\partial x}\Big] + (P_{e,\parallel} - P_{e,\perp})b_y\Big[\frac{\partial b_z}{\partial y}\Big]. \tag{2.17}$$

All the quantities in square brackets, [ ], in Eqs. (2.15)–(2.17) will now be shown to vanish at the separator. As one proceeds to the saddle point (x_o, y_o) of the flux function, $B_x, B_y \to 0$, so that $\mathscr{Q}_I \to 0$. Similarly, since $B_x(x, y_o)$ and $B_y(x_o, y)$ are both minima then $\partial b_x/\partial x, \partial b_y/\partial y \to 0$ and $\mathscr{Q}_{II} \to 0$. Finally, even with a constant guide field $B_z = C$, $\partial b_z/\partial x = \partial b_z/\partial y \to 0$ and $\mathscr{Q}_{III} \to 0$. This calculation shows by contradiction that $\mathbf{P}_e \simeq \mathbf{P}_e^{gyro}$ cannot support the reconnection saddle point of 2-D symmetric reconnection, as it cannot produce the needed E_z dictated by steady state conditions.

Vasyliunas concluded that collisionless magnetic reconnection required a full tensorial $\mathbf{P}_e$, more general than that assumed in Eq. (2.13); this new required generality is sometimes referred to in the literature as the onset of *non-gyrotropy*. Others have adopted the term and symbol *agyrotropy*, $A\emptyset_e$ (Scudder 2008), for this broken cylindrical symmetry, defined by the formula

$$A\emptyset_e = 2\frac{|P_{\perp,e,1} - P_{\perp,e,2}|}{P_{\perp,e,1} + P_{\perp,e,2}}, \tag{2.18}$$

involving the two, possibly different, eigen-values for linearly independent eigenvectors perpendicular to the magnetic field of the tensor given in Eq. (2.35) below. The term *agyrotropy* is a Greek construction that parallels that of *anisotropy*, which is the negation of *isotropy* (Schulz, 2003, private communication); with agyrotropy *an+gyrotropy* collapses to *agyrotropy* since the prefix occurs before a consonant, unlike the case for *an+isotropy*. $A\emptyset_e$ is an observable if the electron pressure tensor is measured in a model independent way with some reports of its detection (Scudder 2008; Scudder et al 2002; Scudder et al. 2012; Lopez 2015; Tang et al. 2013).

Vasyliunas had also noted that achieving an agyrotropic electron pressure tensor would require unusual conditions, since MacMahon (1965) had recently systematized the justification for a gyrotropic pressure tensor provided the electron thermal gyro radius, ρ_e, was small compared to the scale length, L, of gradients in the problem and the time variations of the problem were slow compared to the electron cyclotron period. In the usual MHD ordering, L is presumed much larger than ρ_e; thus the gyrotropic form [Eq. (2.13)] for $\mathbf{P}_e$ assumed in MHD is rarely considered worrisome. However, Vasyliunas' deduction that MacMahon's ordering had to be violated was consistent with his discussing magnetic reconnection where electrons lose their labeling ability of field lines and that magnetic reconnection cannot occur in the relatively weak gradient MHD regimes considered by MacMahon.

Vasyliunas also established that the scale L of the symmetric reconnection layer would be comparable to ρ_e, in order that an agyrotropic $\mathbf{P}_e$ could be understood to naturally occur there. *His analysis made a significant stride in the direction of asserting how MHD's predictions are vacated in the collisionless reconnection layer: disrupt MHD's inherent assumptions about relative scales.* These assumptions are discussed in Sect. 2.4.

In steady state *Vasyliunas's conclusion underscored the importance of measuring short scale lengths in the plasma if reconnection sites are to be identified*. For space measurements this poses serious operational problems (cf. Appendix 3) since the observations are performed in moving media as time series, and are not known along regular cartesian spatial arrays, as are available in a PIC simulation. In addition it is also unknown if the transition is steady, planar, or of a known local orientation. New approaches to this problem are discussed in Sect. 2.4.1 and Appendix 3.

2.3.2.2 Overview Collisionless Description

Since 1975 it has been clear that realizing the correct type of electron pressure tensor to support $\mathbf{R}_{ez}$ at the separator for 2D symmetric reconnection required gradient scale lengths near or under the electron thermal gyro radius. This also meant that the width of the current channel would be of the order of the electron skin depth, since $\rho_e = \beta_e^{1/2} d_e$ and β_e in the current channel is usually $O(1)$. Nearly 25 years later full PIC treatments of the 2D reconnection problem showed from their reconstructed pressure tensors that cylindrical symmetry about the local magnetic field direction was interrupted in the layer thought to be reconnecting (Hesse et al. 1999). As shown in Fig. 2.2 analysis of PIC information also demonstrates that the departure from cylindrical symmetry of the perpendicular eigenvalues $\mathbf{P}_{\perp,e,j}$ of the electron pressure tensor was shown by the enhancements of $A\emptyset_e \neq 0$ near and around X and O points suggested by the projection of field lines from contours of the flux functions; indications of weaker violations of $A\emptyset_e$ along the separatrices are also shown in this figure (Scudder 2008).

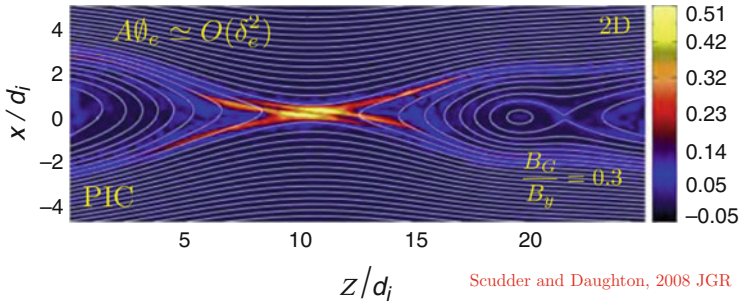

Fig. 2.2 Demonstration of patterns of $A\emptyset_e$ from PIC simulations, demonstrating their ability to label interesting field topologies, indicated with contours of field lines from the flux function. Most intense incidences of $A\emptyset_e$ are shown to radiate from the saddle point. Symmetric weak guide geometry indicated. Nonetheless, enhancements also occur along the separatrices and near O point. *Figure reformatted from* Scudder (2008)

A good portion of the complexity of describing collisionless magnetic reconnection is caused by the theoretically challenging parameter regime of the current channel, possessing kinetic scales: $L_{EDR} < \rho_e \simeq d_e << \rho_i \simeq d_i$. Since the collision times are so long this is also the regime where the plasma transits the scale of the current channel long before coulomb scattering can play a role, making the fluid description and its closure problematic. This parameter regime rules out many traditional descriptions for a plasma, such as two fluid approximations with possible finite Larmor radius corrections, since neither of the species is magnetized. Vlasov fluid treatments simplified by enforcing various invariants along characteristics are also crippled with a heavily restricted number of conserved quantities; for those that can be used they apply only to special geometries. Nothing short of full integration of the self consistent equations of motion for electrons and ions in the evolving electric and magnetic fields is appropriate for theoretical analysis. Fortunately Particle in Cell (PIC) computations are now increasingly being performed in full 3D with modern peta-scale computers. Valiant attempts to extend fluid descriptions into this area have been made, but invariably they are hard pressed to describe the evolution of the pressure tensor well, since the needed *non-local* closures are just not available to truncate these moment hierarchies.

By following the equations of motions of macro electron and proton "particles" and then reassembling their statistical mechanics as a function of space, the PIC approach avoids the irksome problems of closure faced by all reduced closure approaches. The fluid moment equations using the PIC supported plasma moments are then used to understand the phenomena that have been elucidated by eschewing unjustified closure schemes. As with all models there are limitations for PIC models involving number of integration time steps and unwanted collisional effects of macro-particles. With care these limitations can be minimized while making good use of the resolved particle behavior across the narrow current channels.

2.4 2D Reconnection: Training Wheels

In this section thresholded diagnostics are identified for features that can be associated with the inner *electron diffusion region, EDR*. The 2D geometry possesses a built in "ground truth" since it has a flux function that allows the behavior of the in-plane topology of **B** to be interrogated. In particular, the magnetic field in the plane of spatial variations is determined solely by the z component of the vector potential, $A_z(x, y, t)$, which is the flux function. The comoving derivative of A_z in the electron rest frame determines the rate of reconnection (cf. Appendix 1). Contours of $A_z(x, y)$ are field lines (cf. Appendix 1). The description of reconnection in 3D is made more complicated by the *absence* of a flux function when variations in all three dimensions are allowed.

Our approach is to first theoretically show in the controlled 2D PIC environment that *interesting thresholded quantities associated with the defining properties of reconnection are observables*, and then to show visually and statistically that these observable quantities can be used to recover much that the flux function tells the theorist analytically. The advantage is (1) that the physics of these observables is not limited to 2D reconnection, while (2) the leverage of a flux function is a artifice that only works for 2D reconnection modeling, but in 2D it *can* confirm or deny our approach as finding the interesting region where frozen flux is violated. An additional simplification is that the global rate of magnetic reconnection can be determined in 2D geometries from $DA_z/Dt|_{\mathbf{U}_e} = -cR_{ez}$ at the saddle point. In 2D this quantity has been compared favorably (Scudder et al. 2015a) to the frozen flux rate of Eq. (2.7) from Faraday's Law by forming the curls, $\nabla \times \mathbf{R}_e$, directly from PIC variables. While the approach using the curl of $\mathbf{R}_e$ is overkill in 2D, it provides a way in 3D simulations to inventory locales of frozen flux violation where the flux function is not available to help evaluate the value of our thresholded quantities discussed below (Scudder et al. 2015b). As we show in the subsequent sections the observables discussed here also highlight interesting places in 3D and they suggest hints of global conditions of 3D reconnection mentioned in the introduction.

2.4.1 MacMahon and Electron Demagnetization

Vasyliunas' insight suggested that the EDR (in 2D) is a place where MacMahon's systematic expansions for the underpinnings of MHD *fail*. MacMahon's motivation for the commonly used gyrotropic pressure tensor of MHD relied on single particle Guiding Center ordering (Northrop 1963): gyro radius over scale lengths are assumed small and frequencies of time variation described are low compared to the ion cyclotron frequency. In his mathematics there are actually three expansion parameters that are assumed simultaneously small which we will assign the names δ, ϵ and τ. These conditions reduce (MacMahon 1965; Hazeltine and Waelbroeck 1999) to the above casual summary, but *their explicit specification provides one*

immediate benefit: two of them are shown to be observables with the present state of the art instrumentation of space plasma packages.

MacMahon's three assumed small expansion parameters for each species, k, were:

$$\delta_k \equiv \frac{c|\mathbf{E}_{\perp,k} + \mathbf{U}_k \times \mathbf{B}/c|}{w_{\perp,k}B} = \frac{c\left|\mathbf{R}_{k,\perp}\right|}{w_{\perp,k}B} << 1 \tag{2.19}$$

$$\epsilon_k \equiv \frac{2\pi|Z_k e\mathbf{U}_k \cdot \mathbf{E}|}{\Omega_{c,k}kT_k} << 1 \tag{2.20}$$

and

$$\tau_k \equiv \frac{\omega}{\Omega_{c,k}} << 1. \tag{2.21}$$

In the above order these required conditions are that (I) the perpendicular electric force felt in the k'th species rest frame is much smaller than the magnetic force on the thermal speed particle of that species; (II) the energy gain per species gyro period is small compared to the averaged gyrational energy; and (III) the frequency of time variation studied is slow compared to the cyclotron frequency of the k'th species.

Condition III has already been discussed in the beginning of this section, but the ordinary summary for condition I of this regime, $\rho_k/L << 1$, does not explicitly appear in these conditions. Using the electrons as the example, this condition is implied as may be seen by using the leading order term of the Generalized Ohm's law for $en_e\mathbf{R}_e \simeq -\nabla \cdot \mathbf{P}_e$ to restate (I) as

$$\frac{c(I - \hat{\mathbf{b}}\hat{\mathbf{b}}) \cdot \nabla \cdot \mathbf{P}_e}{en_e w_{\perp,e}B} \simeq \frac{< w_{\perp,e}^2 >^{1/2}}{\Omega_{ce}L_\perp} = \frac{\rho_e}{L_\perp}, \tag{2.22}$$

where $L_\perp$ is the cross field scale length has been used to approximate

$$|(I - \hat{\mathbf{b}}\hat{\mathbf{b}}) \cdot \nabla \cdot \mathbf{P}_e| \simeq \frac{n_e m < w_{\perp,e}^2 >}{L_\perp}.$$

It is important to emphasize that relations in Eqs. (2.19)–(2.21) above require the electric field to be measured directly; proxies for the electric field such as $\mathbf{E} \simeq -\mathbf{U_j} \times \mathbf{B}/c$ where the $\mathbf{U_j}$ are either the electron or ion bulk velocity do not contain the information available from a direct, high quality, and calibrated measurement of $\mathbf{E}$. This may be seen since using such an approximation immediately implies that $\delta_j \equiv 0$ yielding the attendant erroneous conclusion that the spatial scales of the system are infinitely large. On the contrary, such an inference is the circular corollary of not introducing ambient information about *all* of $\mathbf{E}$, rather than the ideal

approximations for it that are often used, but contain no sub MHD scale information that characterize plasmas with gradients and reconnection current channels in particular.

Bonus 1: The really good news is that conditions (I, II) *without approximation* are directly measurable with the present state of the art plasma and fields instrumentation in space. Even when $E_\parallel$ is not measured, condition (I) can be determined. Furthermore, δ_k and ϵ_k can be measured *without measuring any lengths, nor determining any geometry as are involved in more traditional length determinations (cf. Appendix 3)*

Bonus 2: This means that *to measure lengths in the plasma one only has to compute the species gyro radius and its form of δ_k, which only requires the measurement of the commonly available $E_\perp$* to infer:

$$L_\perp \simeq \frac{\rho_k}{\delta_k}, \tag{2.23}$$

The hidden sensitivity to length in Eq. (2.23) comes, of course, from having measured the electric field used in δ_k. Accordingly, the length inferred by this process is across the magnetic field. In the ideal MHD limit $\delta_k \rightarrow 0$ and it correctly suggests the scale free MHD world view.

Bonus 3: The form of these dimensionless expansion parameters are interesting for our "thresholdless" problem of the properties that characterize magnetic reconnection, like the violation of the "frozen in condition", $\mathbf{R}_e \neq 0$. The MHD postulates are violated when condition I is violated, which implies

$$\frac{|\mathbf{R}_{e,\perp}|}{B} > \frac{w_{\perp,e}}{c}, \tag{2.24}$$

establishing the values of $|R_{\perp,e}|$ that would seriously violate the *frozen in* condition of MHD. In the solar wind, for example, the RHS of Eq. (2.24) is 0.003. In terms of the wind's thermal Mach number, M_e, we determine

$$|\mathbf{R}_{e,\perp}| > M_e^{-1}|\mathbf{E}_{\perp,sw}| \simeq 10\, mV/m, \tag{2.25}$$

where we have assumed $U = 400\, km/s$, $B = 5\, nT$ and $M_e = 0.2$, which are all typical in the solar wind. In this same regime the perpendicular components of the divergence of $\mathbf{P}_e$ would suggest $|\mathbf{R}_{e,\perp}| \simeq 10^{-7}|\mathbf{E}_{\perp,sw}|$; thus, it would be difficult to satisfy Eq. (2.25) in the solar wind proper. The principal reason for this circumstance is the half AU scale length of the electron pressure in the unstructured solar wind.

Bonus 4: The energy gain expansion parameter ϵ_k constrains parallel and perpendicular parts of $\mathbf{R}_e$, viz

$$\epsilon_k = \frac{4\pi c}{w_{\perp,k}B}\left(\mathbf{M}_{k,\perp}\cdot\mathbf{R}_{k,\perp} + M_{k,\parallel}R_{k,\parallel}\right) << 1 \tag{2.26}$$

where $M_{k,q}$ is the q'th component of the electron thermal mach number of the flow. It should also be noted that with MHD ordering the first term in Eq. (2.26) is formally zero; however, in the EDR this term *can* be important and must be retained for exploration for circumstances where $\epsilon > 1$. (However, if this first term is experimentally found to be important away from current channels there are experimental errors in the observables used, since routinely this quantity should be consistent with experimental zero.)

Equation 2.26 can be rewritten as a condition on how big a parallel electric field can be before violating the MHD ordering. Using k = e for specifics

$$\epsilon_e = 4\pi\delta_e \left| \mathbf{M}_{e,\perp} \cdot \hat{\mathbf{R}}_{e,\perp} + M_{e,\parallel} \frac{E_\parallel}{|\mathbf{R}_{\perp,e}|} \right| << 1. \tag{2.27}$$

Clearly the limit of Eq. (2.27) on $E_\parallel$ is proportional to $|\mathbf{B}|$, being proportional to δ_e^{-1}. Thus, detections of $E_\parallel$ "bigger than my instruments sensitivity level", while interesting, are not sufficient to show that MHD ordering is violated until $\epsilon_e > 1$ is demonstrated. Such limits will be different in the magnetotail than at the forward magnetopause, or auroral zones.

The other insight from this form is that MacMahon's parameters are potentially interdependent when $\delta_e \simeq 1$ and the non-ideal electric field and electron flow are not orthogonal. Within the current channel evidence exist from PIC that ϵ_e and δ_e can be correlated, but generally are not as MHD ordering becomes more prevalent and δ_e relaxes to zero, attended by $\mathbf{E}_\perp \cdot U_{\perp,e} \to 0$.

Bonus 5: For frozen flux slippage to be innocuous its time scale should be slow compared to the electron cyclotron frequency

$$\frac{\nu_\Phi}{\Omega_{ce}} = \left| \frac{-c \oint\!\!\oint_C \hat{\mathbf{b}} \cdot \nabla \times \mathbf{R}_e da}{< B > A\Omega_{ce}} \right| \simeq \rho_e \frac{\delta_e}{L_{\nabla\times}} \simeq \delta_e^\alpha << 1, \tag{2.28}$$

where Eq. (2.23) has been used and the scale of the gradients of the curl indicated by $L_{\nabla\times}$. If this scale is estimated also from the gyro radius and Eq. (2.23) then $\alpha \to 2$ in Eq. (2.28) . If the $L_{\nabla\times}$ saturates at ρ_e, then $\alpha \to 1$. Equation 2.28 is in the form of the τ condition III of MacMahon [cf. Eq. (2.21)]. As shown below in Fig. 2.22 electron agyrotropy has just the same scaling, $A\emptyset_e \propto \delta^\alpha$, flipping between 2 and 1 as agyrotropy intensifies.

Thus, Eq. (2.28) can be rewritten in a form that clearly restates Vasyliunas' insight, but now from the vantage point of 3D:

$$\frac{\nu_\Phi}{\Omega_{ce}} \sim A\emptyset_e. \qquad (3D) \tag{2.29}$$

The arguments leading to Eq. (2.29) also suggest that MacMahon's condition III is also rendered "observable" through $A\emptyset_e$. We define the observable $\Upsilon_{*,\Phi} \equiv \Omega_{ce} A\emptyset_e$ and have calibrated $\Upsilon_{*,\Phi}$ against direct determination of ν_Φ in a 3-D PIC simulation to determine the scaling of Eq. (2.29) to be

$$\nu_\Phi = 0.80 {\Upsilon_{*,\Phi}}^{0.685} \equiv \Upsilon_\Phi(\Omega_{ce}, A\emptyset_e) \tag{2.30}$$

In this way the new quantity Υ_Φ becomes a *calibrated observable proxy in 3D* for the *unobservable* rate ν_Φ of frozen flux violation.

Bonus 6: Another possible measure for thresholding the *strength of the violation of frozen flux* that has recently been used with PIC codes is

$$\Lambda_\Phi \equiv \left| \frac{\nu_\Phi}{Dln\nu_\Phi/Dt|_{\mathbf{U}_e}} \right| \propto \frac{\sqrt{3}\nu_\Phi}{\Omega_{ce}\delta_e M_e cos\Theta\sqrt{2+An_e}} \equiv \Psi_{*,\Phi}. \tag{2.31}$$

In this expression An_e is the electron anisotropy, and $cos\Theta$ is the dot product between unit vectors of the electron's flow and spatial derivatives in the convective derivative in the denominator of the definition of Λ_Φ. The motivation for the form for Λ_Φ is that

$$\Lambda_\Phi \simeq \frac{\nu_\Phi}{\nu_{transit}} = \frac{\tau_{transit}}{\tau_\nu} \tag{2.32}$$

determined by the ratio of the time scale, $\tau_{transit}$, for the electron fluid to transit the scale of the local frozen flux violations to the time scale of the frozen flux violations, τ_ν . The idea behind this condition is that it takes time for the electron mechanics to react to the frozen flux violation which already measures these violations in its rest frame. The natural yardstick for ν_Φ is then the rate $\nu_{transit}$ at which these violations were traversed. It is conceivable that narrow regions of extreme frozen flux violation can be rendered innocuous by passing across them rapidly; or, conversely that slow traverses can enhance slow rates of frozen flux violations. This approach explicitly acknowledges that weak frozen flux violations may not be informative for the location of reconnection sites, where we have shown that frozen flux violations are substantial, that is with $\Lambda_\Phi > 1$.

Finally, theoretically thresholded Λ_Φ is rather difficult to evaluate directly even from PIC variables; by consensus Λ_Φ is unmeasurable using the current state of the space instrumentation (since ν_Φ is). However, the extreme RHS of Eq. (2.31) suggests a test for an *observable* proxy between Λ_Φ and an observable ratio, $\Psi*_\Phi$, given by

$$\Psi_{*,\Phi} = \frac{\sqrt{3}A\emptyset_e}{\delta_e cos\Theta M_e\sqrt{2+An_e}}, \tag{2.33}$$

that does not require curls of $\mathbf{R_e}$ for its evaluation, but requires a well calibrated electron detector on a single spacecraft. Studies of the correlation between $\Psi_{*,\Phi}$

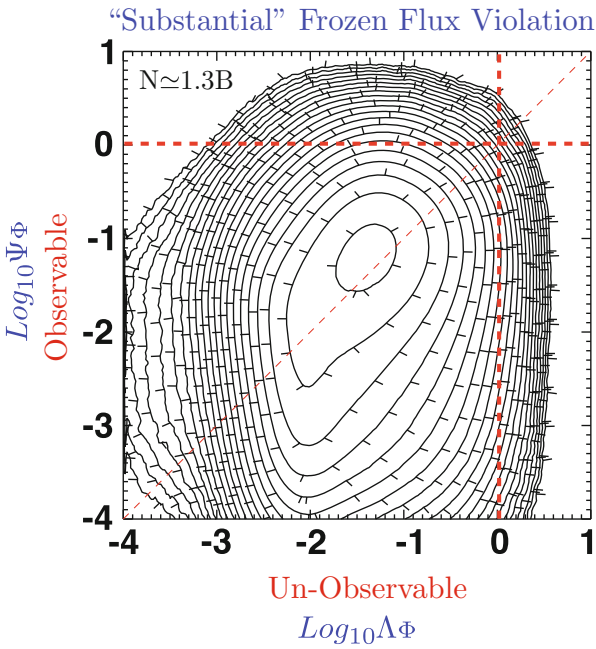

Fig. 2.3 Correlation from 3D PIC between the observable Ψ_Φ and the unobservable Λ_Φ that when greater than unity locally identifies regions of strong frozen flux violation that appear to be necessary at a 3D reconnection site. From forth coming reference Scudder et al. (2015b)

and Λ_Φ using 3D PIC codes have determined the following calibrated form for this proxy:

$$\Psi_\Phi \equiv \left(\frac{\Psi_{*,\Phi}}{18.13}\right)^{1.921} \simeq \Lambda_\Phi, \tag{2.34}$$

which shows that $\Psi_{*,\Phi}$ tends to overestimate the desired size of Λ_Φ; the calibration afforded by Eq. (2.34) can be used with observables to emulate the unmeasurable Λ_Φ. The precise constants of this correlation are specific to the resolution of the PIC simulation used. The correlation between $Log_{10}\Psi_{*,\Phi}$ and $Log_{10}\Lambda_\Phi$ is also very strong, but is not calibrated for determining sites of $\Lambda_\Phi \simeq 1$. The excellent correlation Ψ_Φ, Λ_Φ using Eq. (2.34) is shown in Fig. 2.3 which was performed with over 1.28 billion determinations across the entire 3D PIC simulation discussed below. A flotilla's measurements of Ψ_Φ could help delineate the context of the regime as shown below with Fig. 2.18.

2.4.2 "Observations" in 2D PIC of ν and Λ

An example of using these diagnostics is shown in Fig. 2.4, where color contours of frozen line violation, $\nu_\uparrow$ and thresholded values of $\Lambda_\uparrow$ variation are shown from a 2D anti-parallel PIC simulation. White curves denote projections of magnetic field

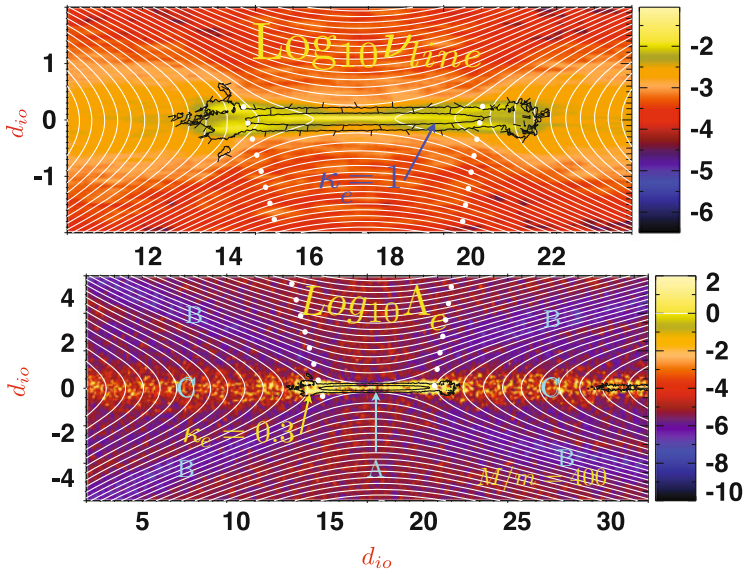

Fig. 2.4 *Top*: Colored contour shows $Log_{10}\nu_{\uparrow}$ with superposed contour (*black*) of $\kappa_e = max\{\delta_e, \epsilon_e\}$ in *black* with downhill direction indicated by flags. (*B*): Same region in larger context, with the same isocontours of κ_e indicated on top of $Log_{10}\Lambda_{\uparrow}$. The *color contours* in *Bottom* are determined by operations that may be performed on 3D simulations. When $\Lambda_{\uparrow} > 1$ this method finds the saddle point (known here in 2D) to be the reconnection locale. The *black contours* also show that MacMahon's assumptions are strongly violated in the same vicinity of the saddle point. The κ_e diagnostic and $\Lambda_{\uparrow}$ reenforce one another's implications. *Reproduced with permission for the November 2015 Phys. Plasmas, **22**, 101204, Copywrite 2015, AIP Publishing LLC* (Scudder et al. 2015a)

lines in the plane of variations. Larger values of both variables are concentrated near the saddle points indicated by the field curves, but extend well away from them in certain directions. Isocontours of $\kappa_e = max\{\delta_e, \epsilon_e\}$ at 0.3 and 1 are superposed in black on the color contours (flags denote the downhill direction); they clearly encircle the saddle point indicated by the pattern of the projections of the magnetic field. The contiguous region of enhanced demagnetization, $\kappa_e > 1$, clearly envelopes the peak region of descending intensity of $\nu_{\uparrow}$ and clearly frames the region of $Log_{10}\Lambda_{\uparrow} > 0$ which is where $\Lambda_{\uparrow} > 1$. The contours of $\Lambda_{\uparrow} = 1$ also clearly differentiate between *innocuous* and significant frozen flux violations, agreeing that the important regions encircle the saddle point from the flux function and pointing to the complementary regions as being innocuous. $\Lambda_{\uparrow}$ out along the separatrices and in the exhaust of the reconnection patterns are several power of 10 below its above unity size near the saddle point. The frozen flux slippages along the separatrices, while present, are thus anecdotal, and do not suffice to identify the separatrices as reconnection sites. *The flux function underscores the correctness of this inference.* Nonetheless, there are *some* hints of demagnetization in the vicinity of the separatrices, reenforcing the insufficiency of reporting

non-zero demagnetization, by itself, for identifying regions where significant frozen flux violations, as is occurring when $\Lambda_{\uparrow} > 1$ about the saddle point. We return to this point in the discussion section.

While the pattern of theoretically interesting color contoured variables in this figure can be determined with PIC variables, they are *presently unobservable* using present state of the art measurements from space platforms. Only the information involving δ_e and ϵ_e that went into determining the black contours of the thresholded demagnetization condition, κ_e, are observables. This figure demonstrates that these observables do provide needed information for diagnosis of such regions; however, even the *topography* of κ_e is not a direct observable. As a scalar $\kappa_e(t)$ would be ready observable; using a flotilla of spacecraft measuring κ_e simultaneously perhaps the variation of $\kappa_e(\mathbf{x})$ might be inferred for limited areas. Being dimensionless and with some background in PIC studies of this type (as a function of guide field strengths and asymmetry) *in situ* diagnosis of regimes may be facilitated.

2.5 Macro Signatures of Demagnetized Electrons

The signatures of electron demagnetization just discussed involve using measurements of the electromagnetic field components in the electron rest frame. The indices of electron demagnetization imply thresholds for the size of $|\mathbf{R}_{e,\perp}|/B$ and $E_{\parallel}/B$. *In this section we deduce further moment level corollaries of demagnetized layers that can be assessed without measuring the electric field* and refer the reader to recent more detailed examples in the literature (Scudder et al. 2015a,b; Scudder 2015).

2.5.1 Agyrotropy $A\emptyset_e$

A way to detect agyrotropic electrons is to compute the symmetric tensor which measures the average velocity space variance of the distribution function perpendicular to the magnetic field direction:

$$\aleph_{ij} = < (\mathbf{w} \times \hat{\mathbf{b}})_i (\mathbf{w} \times \hat{\mathbf{b}})_j >, \tag{2.35}$$

where $\mathbf{w}$ is the electron velocity in the electron rest frame and $<>$ stands for a velocity space average over a temporally unaliased velocity distribution. Such measurements are best performed by detectors that do not wait for the sensors to reorient by one half spin to obtain their full solid angle coverage. This tensor has only two non-zero eigenvalues, since the third vanishes with the magnetic field as its eigenvector. If its two non-zero eigenvalues are not equal the distribution is certainly

not gyrotropic. As shown in Scudder (2008) the two non-zero eigenvalues of $\aleph$ are given by

$$\lambda_{\pm} = \frac{\alpha \pm \sqrt{\alpha^2 - 4\beta}}{2}, \tag{2.36}$$

where $\alpha = Tr\,\aleph$ and

$$\beta = -(\aleph_{xy}^2 + \aleph_{xz}^2 + \aleph_{yz}^2 - \aleph_{xx}\aleph_{yy} - \aleph_{xx}\aleph_{zz} - \aleph_{yy}\aleph_{zz}). \tag{2.37}$$

Then agyrotropy, $A\emptyset_e$ is defined to be

$$A\emptyset_e = 2\frac{|\lambda_+ - \lambda_-|}{\lambda_+ + \lambda_-}, \tag{2.38}$$

which ranges between the gyrotropic limit of 0, and the planar limit of 2. For this measurement to be geophysically interesting its size must routinely be demonstrated to be small and only enhanced in layers with current channels as implied by the magnetic field profile. The experimentally routine values of $A\emptyset_e$ away from current channels reflect the state of calibration of the detection system and *must* be established prior to "detection" of $A\emptyset_e \neq 0$.

An alternative characterization of electron demagnetization is sensed by the size of the irreducibly tensorial part, χ, of the electron pressure tensor, $P_{e,ij}$, defined by the operation

$$\chi \equiv P_{e,ij} - ab_ib_j - \frac{(Tr\mathbf{P}_e - a)}{2}(\delta_{ij} - b_ib_j), \tag{2.39}$$

where $a = \hat{\mathbf{b}} \cdot \mathbf{P}_e \cdot \hat{\mathbf{b}}$. If the plasma is gyrotropic χ is the null matrix. There are many ways to judge the *size* of a matrix. The matrix χ essentially describes the variations of the pressure different from being cylindrically symmetric about $\mathbf{b}$. As a matrix χ contains information about the symmetry breaking in three eigen-directions that have no a priori connection to $\mathbf{b}$. Unless those eigen-directions are computed, inventories of the size of this symmetry breaking are not unique.

A scaled version of the Frobenius norm of χ has also been suggested to estimate the size of χ (Aunai et al. 2013). The Frobenius norm of χ is the square root of the sum of the squares of its eigenvalues and the recently proposed alternative for $A\emptyset_e$ is

$$Au_e = \frac{2\sqrt{\Sigma_k \lambda_k^2}}{Tr\,\mathbf{P}_e}. \tag{2.40}$$

Other equally frame invariant measures that *could* be used to measure the departures represented by χ are the geometric mean of the absolute value of the eigenvalues

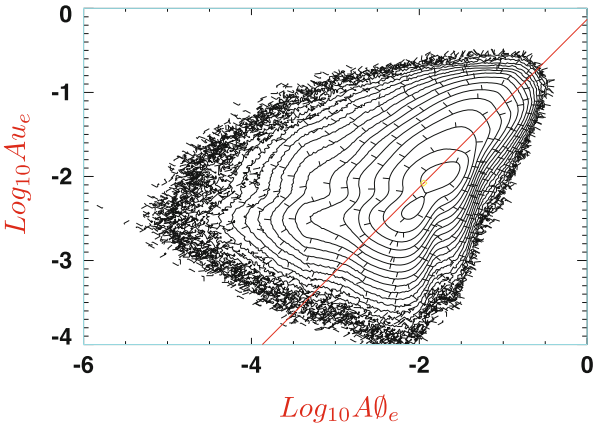

Fig. 2.5 Correlation of $A\emptyset_e$ and Au_e showing that these two apparently different measures are generally in agreement, especially for the bigger values. To guide the eye the *red line* i$y = x + x_o$ is included with origin set by the highest probability point in the 2D histogram. From forthcoming reference Scudder et al. (2015b)

compared to the average eigenvalue of $\mathbf{P}_e$

$$Au_{e2} \propto \frac{3\sqrt[3]{|Det\ \chi|}}{TrP_e} \tag{2.41}$$

or the straight ratio of determinants of χ and that of the entire pressure tensor:

$$Au_{e3} \propto \frac{|Det\ \chi|}{Det\ \mathbf{P}_e}. \tag{2.42}$$

Figure 2.5 shows the correlation of $A\emptyset_e$ and Au_e using over 1.28 billion estimates in a 3D asymmetric guide example (Daughton et al. 2011), showing that the two proposed indices of agyrotropy produce very similar information, especially when the selected observables are largest.

2.5.2 *Electron Thermal Mach Number*

To achieve a narrow, electron inertial scaled current channel the electrons of the plasma must almost exclusively support the out of plane current density, because the ions are not nimble enough to do so. As derived in Scudder et al. (2015a) Ampere's equation implies that the electron thermal Mach number, M_{ez}, in the out of plane current channel should be of order unity, or more precisely

$$M_{ez} \sim \frac{\delta_e}{\beta_e\sqrt{1+S^2}} \tag{2.43}$$

where S is the ratio of guide field to interconnection field strength well away from the current sheet. Equation 2.43 is derived assuming the magnetic profile is linear

near its reversal with a scale L suggested by the crossing orbits of the electrons. The scale of the current has been taken to be $L = \sqrt{d_e \rho_e}$, motivated by Parker's early considerations of particle dynamic studies at current sheets (Parker 1957); the electron β_e in this formula is determined at the scale length L from the null using the reconnecting components of **B** only. Various combinations of $\delta \simeq 1$ and $\beta_e \uparrow 1$ suggest that M_e could be order unity within the current sheet.

For the experimentalist *detection of* $O(1)$ *electron thermal mach numbers represent a truly unusual circumstance*, since even the *supersonic* solar wind only has $M_e \simeq 0.2$, and that value is reduced upon entering the sheath as the flow speed is reduced and the thermal speed increased. (Here too, the routine agreement of $\mathbf{U}_e \simeq \mathbf{U}_i$ must be experimentally demonstrated for comparable density and temperature regimes before the detection of large M_e is defensible.) In the one resolved electron diffusion region reported to date $M_e > 1$ was reported (Scudder et al. 2012) as reproduced below in Fig. 2.13.

2.5.3 Convergent Electric Fields

Models of reconnection invariably have converging electric fields caused by the *unmeasurable* space charge in the layers that exist to induce the ions to come towards the separator. These electric fields are concentrated normal to the current sheet and are perpendicular to the guide and interconnection magnetic field components. These fields are usually strong as compared with MHD electric fields, but their ability to demagnetize electrons depends on $\delta_e > 1$. This demagnetizing condition becomes $E_\perp > B(nT) w_{\perp,e}/c$, which in observational units implies

$$E_\perp(mV/m) > 0.55 B(nT) \sqrt{T(eV)}. \tag{2.44}$$

At the magnetopause this condition becomes (with 50 nT and 100 eV) a threshold for demagnetization of approximately $E_\perp > 275\, mV/m$, while the MHD inflow reconnection electric field at $U_{in} \simeq 0.1 M_A$ has a size of $E_{recon} \simeq 2.5\, mV/m$. Macroscopically, the convergent pattern (cf. inset (c) Fig. 2.8) is unusual correlative information. Before reaching their peak strengths such fields will cause electric drifts in the electrons, until disrupted by their demagnetization.

As distinctive as the convergent electric field pattern may be, the inference of electron demagnetization from this asymmetric pattern would require measuring values of $E_\perp$ more than 100 times the reconnection MHD electric field. In the presence of asymmetric reconnection with $B_{sh} < [1 - 4] B_{sp}$ the measured normal electric field is also asymmetric with $|E_{x,sh}| < |E_{x,sp}|$. The observations are consistent with comparable, but very small, demagnetization on the two sides of the current channel. Below, symmetric and asymmetric current layers are illustrated that show this range of asymmetries in the converging electric field strengths.

2.5.4 *Electron Anisotropy*

In the layers adjoining the low density side of the electron diffusion region there is a zone where the electrons, though still magnetized, are bouncing back and forth in a parallel electrical potential, gaining energy from the parallel electric field while moving into a weakening magnetic field. Conservation of the first adiabatic invariant causes rather large electron anisotropies to occur *while the electrons still remain magnetized*, again because the numerator of μ is increased while the denominator decreased. Electron anisotropies as high as 8–10 are seen in PIC simulations (Le et al. 2009; Egedal et al. 2012). A recent resolved EDR gave evidence for electron temperature anisotropy of nearly 8 (Scudder et al. 2012) shown in Fig. 2.13 below.

2.6 Overview of Observables

The relationship of our thresholded observables and theoretical quantities of magnetic reconnection are identified in Fig. 2.6; in addition, the logical progression of these techniques from 2D into 3D geometries is also shown. Proceeding from left to right we have shown that the comoving time rate of change of the flux function, $\frac{DA_z}{Dt}|_{\mathbf{U}_e}$, agrees with the reconnection rate determined from Eq. (2.7) in 2D simulations (Scudder et al. 2015a). With 2D simulations we can determine the rate using the 2D peculiar flux function approach and via the $\nabla \times \mathbf{R}_e$ and Eq. (2.7), which is available in either 2 or 3 dimensions. We then show that the region of enhanced ν_Φ agrees with the saddle point of the flux function. We also see that this same

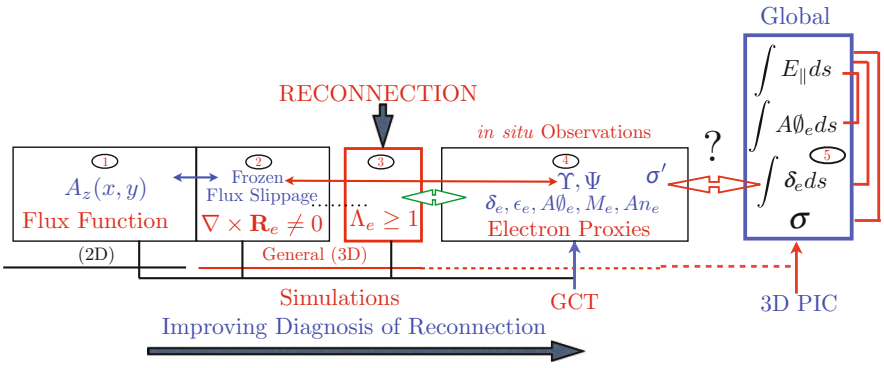

Fig. 2.6 The links between theoretically interesting quantities (boxes 1–3), and observable ones including the new ones (box 4), Υ and Ψ proposed in Scudder et al. (2015a) to generalize the determination of the local rate of frozen flux violation and its significance in 3D. Far *right rectangle* (5) suggests some *global* theoretical diagnostics of interest, including the squashing index σ that we suggest has an observable proxy, σ', in this chapter. See text. *From forthcoming article* Scudder et al. (2015b)

region is one where δ_e and ϵ_e are misordered, showing that the thermal electrons are demagnetized there. In box 3 we explore with Λ what is the necessary threshold for ν_Φ to be big enough to be "dynamically important" and thus indicative that the observer is in the region like the X point region of 2D reconnection. Box 4 correlates the evidence for the primary and secondary signatures of electron demagnetization with this conclusion both in 2D and 3D simulations. In box 5 we briefly touch on local signatures of global squashing σ properties that are beginning to be explored with 3D PIC simulations.

2.7 Benchmarking Thresholded Observable Quantities

In 2D simulations the flux function conveniently summarizes the changing topology of **B** projected on the 2D plane of variations. With the flux function information (available in PIC) as a backdrop, we now look at the thresholded *observable* spacecraft diagnostics deduced from PIC simulations to show that they, too, can find what the flux function knows all too well. The idea is that in 3D there is no flux function, so these new diagnostics (which do not depend on the dimensionality of the reconnection layer being studied) have the potential to supply auxiliary information (usually provided by the flux function in 2D) that can be accessed when studying 3D sites occurring in PIC or nature. In addition, the ability to locally determine ν_Φ via the $\nabla \times \mathbf{R}_e$ gives us a control (like the flux function) that can be determined in 3D simulations to have an idea where frozen flux violations are taking place and, by transitivity, to evaluate the thresholded quantity Λ_Φ's ability to label regimes where demagnetization is dynamically important.

Our approach in this initial sub-section analyzes frames from 2D PIC simulations of anti-parallel reconnection, where a flux function is available, to show that $\delta, \epsilon, \Lambda$ contain information similar to that reflected in the flux function.

2.7.1 2D Anti-Parallel

The thresholded guiding center theory expansion variables of Eqs. (2.19)–(2.21) for an anti-parallel simulation are shown in Fig. 2.7 with the 2D *projections* of the magnetic field lines (white) superposed. This column of contours is framed at the top by the *unobservable* rate of frozen line violation $\nu_\uparrow$ and its dimensionless variant, $\Lambda_\uparrow$ (bottom). The domain of vigorous frozen line violation occurs when $Log_{10}\Lambda_\uparrow > 0$. In the top panel black contours of $\kappa_e = \max\{\delta_e, \epsilon_e\} = [0.3, 1]$ are superposed with flags that point "down" hill. These contours, indicative of strong electron demagnetization, neatly enclose the region of maximum $\nu_\uparrow$, as well as the yellow regions in the bottom panel where $\Lambda_\uparrow > 1$. According to our 3D capable approach the bottom panel suggests that dynamically important frozen flux violations occur where $\Lambda_\uparrow > 1$ in precisely the same locations where the observable

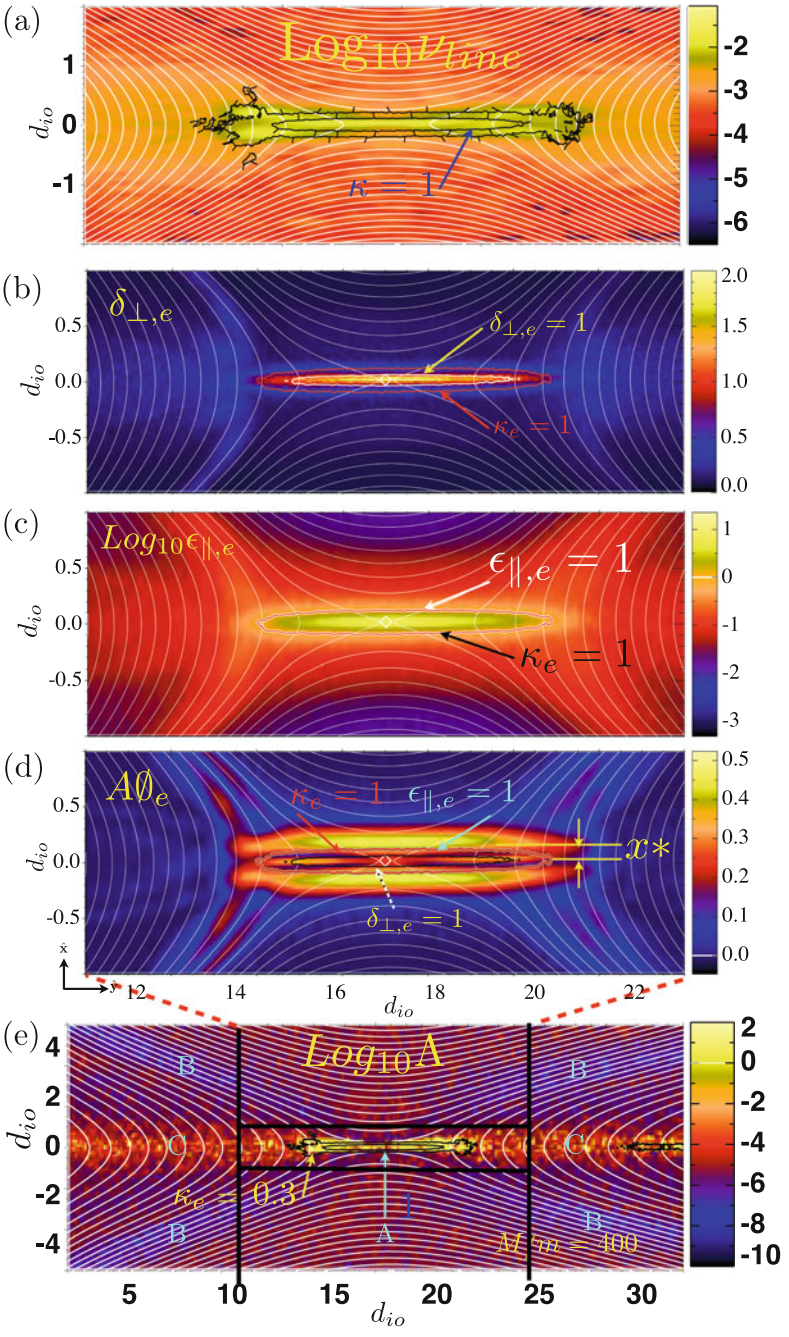

Fig. 2.7 Microscopic signatures of electron demagnetization from reference Scudder et al. (2015a). See text for description. Note the differential compression 6:1 of the horizontal and vertical axes. Anti-parallel, open PIC simulation of reconnection with $d_{io} = 20d_{eo}$. Separate panels discussed in text. *Reproduced with permission for the November 2015 Phys. Plasmas,* ***22****, 101204, Copywrite 2015, AIP Publishing LLC* (Scudder et al. 2015a)

MacMahon indices of demagnetization are significant, and in a saddle point region of the 2D available flux function.

The middle three panels of Fig. 2.7 are all *observables*: MacMahon's first two perturbation parameters clearly show they are not small compared to unity in the saddle point region. The third panel is visual proof of Vasyliunas' deduction that agyrotropic $\mathbf{P}_e$ is required in this saddle point area for collisionless reconnection to occur. The double ribbon pattern of $A\emptyset_e$ seems to reflect a spatial localization of demagnetization as if the outer ribbons are turning points in orbits that concentrate agyrotropic disruptions of phase space density. The channel of large δ, for example, is narrower than is the double ribbon of $A\emptyset_e$. Since the channel has scales well under the gyro radius the consequences for the fluid moments and the pressure tensor will be felt over a broader spatial scale commensurate with where the electrons begin to sense the field again. This can be seen better in Fig. 2.9 where the true maximum peak of the ribbons of $A\emptyset_e$ occur rather precisely when $\kappa_e < 1$, which reflects the increasing magnetization of the disrupted electrons leaving this inner area.

These data support the idea that the saddle point area where significant frozen flux violation is occurring (using $\nabla \times \mathbf{R}_e$) are places where the electrons are indeed demagnetized, while identifying the same locale where the flux function has a saddle point.

Manifestations at the macroscopic moment level of underlying circumstances where the electrons are demagnetized are shown in Fig. 2.8. The top panel shows the strongly varying electron thermal mach number, peaking near $M_e \sim O(1)$, that reflects the electron inertial scaled current channel and that the ions cannot contribute significantly to the drift. This signal is so extraordinary that it should be routinely expected if a case is to be made that the EDR has been traversed; such a strong signature is not known to occur elsewhere where *in situ* samples of astrophysical plasmas have been made; even through shock waves $M_e << 1$ is typical. The anisotropy signature (e) is not directly that of demagnetization of the electrons, but the reverse: it reflects the manipulation of the pressure anisotropy by the strong parallel electric field along the separatrices coupled with electrons cooling as they move into weaker magnetic fields. The principal signature is the unusually large pressure anisotropies compared to that more typically seen in well sampled locales such as the solar wind, magnetosheath or magnetosphere, where electron anisotropies are rarely outside of the range $0.5 < An_e < 2$. If larger electron anisotropies than this range are encountered when crossing current channels indicated by **B**, they should be evaluated for evidence of an exit from a demagnetized region. In the antiparallel geometry, as here, these layers can be seen on both "sides" of the current sheet, whereas they occur preferentially on the low density side of asymmetric reconnection layers, especially favoring low β_e and guide geometries (cf. Sect. 2.7.2, Fig. 2.10). The middle three panels illustrate other features of the layer: (1) their departure from charge neutrality (b), although this is not presently thought to be observable; (2) the pattern of converging electric fields along the inflow normals which has been observed (c). These converging electric fields owe their size to the space charge in the layer, but they appear also to be causative of the agyrotropy seen in the electrons (which is contoured on top of the colored E profile).

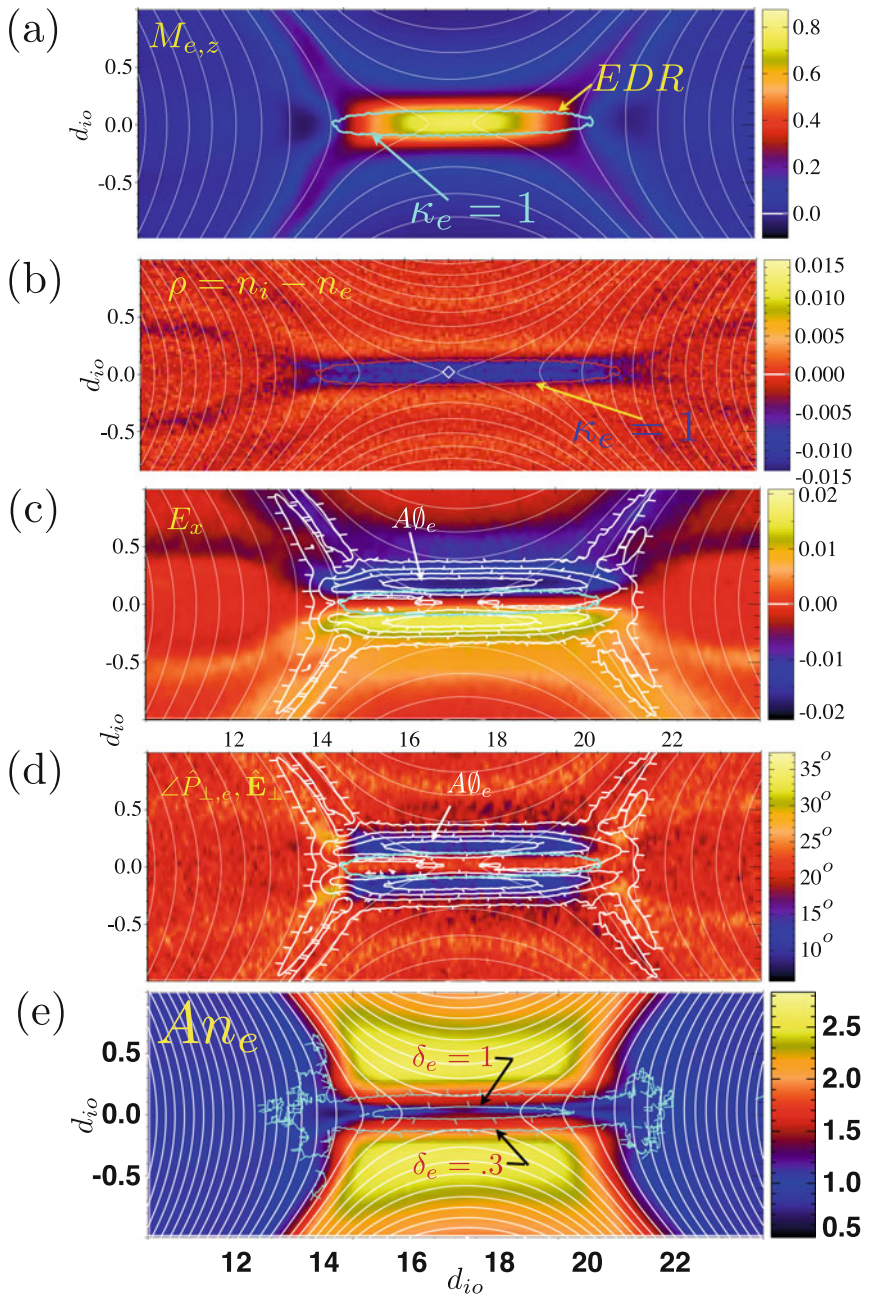

Fig. 2.8 Macroscopic observables associated with the reconnection layer as discussed in the text; same data as in Fig. 2.7. *Reproduced with permission for the November 2015 Phys. Plasmas, **22**, 101204, Copywrite 2015, AIP Publishing LLC* (Scudder et al. 2015a)

The short scales of the transition and the strong electric field allow this electric field to do work on the gyro motions of the electrons. Ordinarily crossed **E** and **B** fields cause electrons to $\mathbf{E} \times \mathbf{B}$ drift, provided the electrons remain magnetized which they do not across the EDR. In such a regime all components of **E** can do net work on the electrons and contribute to ϵ_e.

An observable indication of this effect at work is to compute the angle θ between the perpendicular electric field and the nearest perpendicular eigenvector of pressure tensor (d). Commonly $\theta << 25°$ in regions when $A\emptyset_e$ is seen to be enhanced. This same condition allows the perpendicular electric field to enhance ϵ_e, thus keeping this index high, reflective of it being disordered with respect to MacMahon's assumptions. (See Scudder 2008 for more details.)

The simultaneous profiles of the reconnection layer along the inflow and outflow symmetry lines are provided in Fig. 2.9. Comparing the top and bottom panels allows the ratio of inflow to outflow region of demagnetization to be determined for this symmetric anti-parallel case. Using $\kappa_e \simeq 1$ one determines a ratio of integrated full widths for inflow to outflow to be $1.75d_e : 48d_e$, which is $1.75d_e : 2.4d_i$, where local skin depths have been used to account for the variation of the density across the profile. The abrupt decrease in the $\kappa_e < 1$ along the exhaust signals the remagnetization of the electrons in the exhaust. This accompanies a strong braking of the electron's exhaust flow speed as they must now *respect and gyrate* about the strengthening normal magnetic field across the exhaust. This braking also causes some electron heating to occur (not shown) and is the cause of the two zone picture of the outflow region of the EDR (Karimabadi et al. 2007).

2.7.2 2D Symmetric Guide Geometry Diagnostics

Diagnostics for the 2D symmetric guide geometry are also shown in the panels of Fig. 2.10, where a guide field 0.5 that of the interconnecting magnetic field is used with mass ratio 360. The out of plane guide field adds a new asymmetry to the electrodynamics that is especially clear across the exhausts where a *preferred* separatrix line occurs, so that of the two lines that define the separatrices, one of them becomes preferred and negatively charged as a result of the newly remagnetized electrons in the exhaust feeling a $-|e|\mathbf{U}_e \times \mathbf{B}_{guide}/c$ force that rather promptly encourages the electrons in the exhaust to veer up against the preferred separator. This process leaves the full width of the exhaust with a non-uniform character, with more electrons to one side than the other. The ions are not as magnetized in the exhaust, nor are they travelling initially as fast as the electrons, so there is a polarization of charge. This separation of charges causes a secondary electric field across the exhaust, which with the guide field, produces a large scale component of E×B along the exhaust that assists in bring the ions up to their terminal Alfvén speed as they become demagnetized. The exhaust channel for the electrons is asymmetrically confined to the vicinity of, but inside of, this preferred separatrix arm whose location is delineated by the flux function.

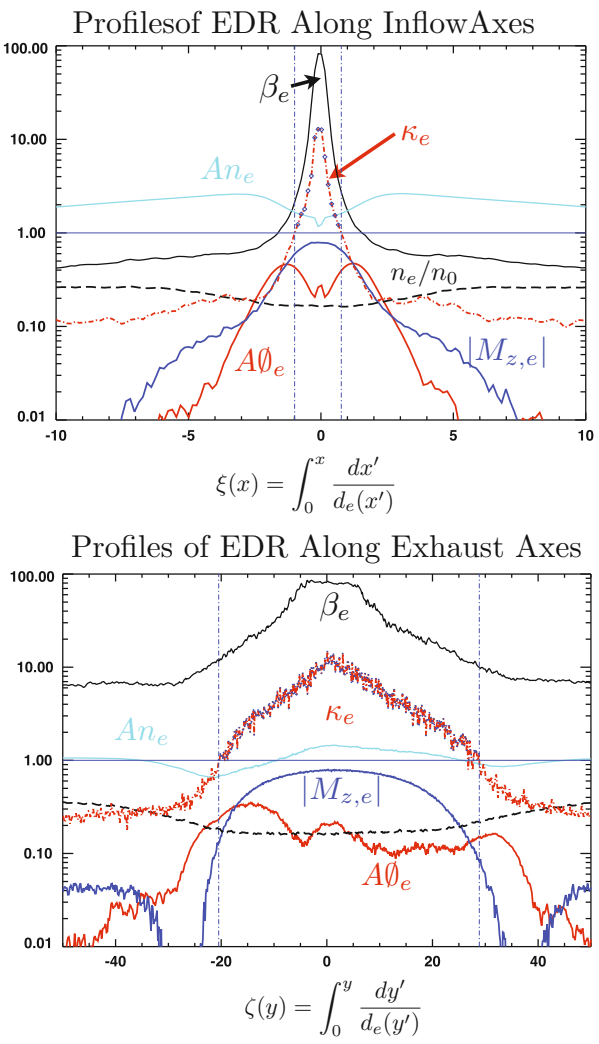

Fig. 2.9 *Top* Diagnostic profiles on inflow symmetry axis; *Bottom* on exhaust symmetry axis of Fig. 2.8. *Reproduced with permission for the November 2015 Phys. Plasmas, **22**, 101204, Copywrite 2015, AIP Publishing LLC* (Scudder et al. 2015a). $d_{io} = 20d_{eo}$ in this simulation

The presentation shows a mixture of diagnostic quantities across the plane (Fig. 2.10) and then focuses in Fig. 2.11 on statistically histogrammed properties found in the layer (defined by the dotted lines in Fig. 2.10d) inside the exhaust separatrix known from the flux function.

The statistics show that peak values of MacMahon's $\epsilon_e > \delta_e$, but that there is a strong demagnetizing spike near the center of the preferred arm superposed on a generally enhanced demagnetization along the preferred arm, including general enhancements of $A\emptyset_e$. Throughout and along the preferred arm significant frozen flux slippage is seen as in our LHDI simulation in Fig. 2.14 below. In agreement with the flux function's assessment of the topology, our thresholded level Λ remains

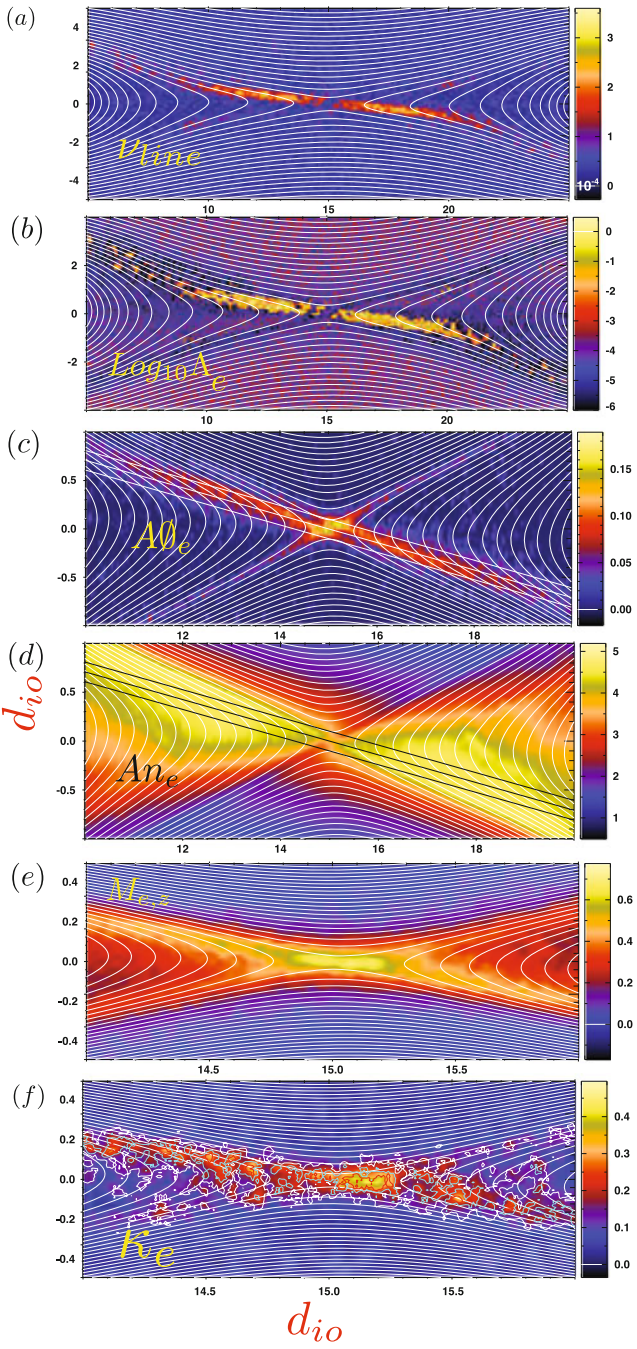

Fig. 2.10 Diagnostics of 2D Guide geometry S=0.5 as discussed in the text. Diagonal lines indicate region where further details and diagnostics are presented in Fig. 2.11. *Reproduced with permission from the November 2015 Phys. Plasmas,* ***22****, 101204, Copywrite 2015, AIP Publishing LLC* (Scudder et al. 2015a)

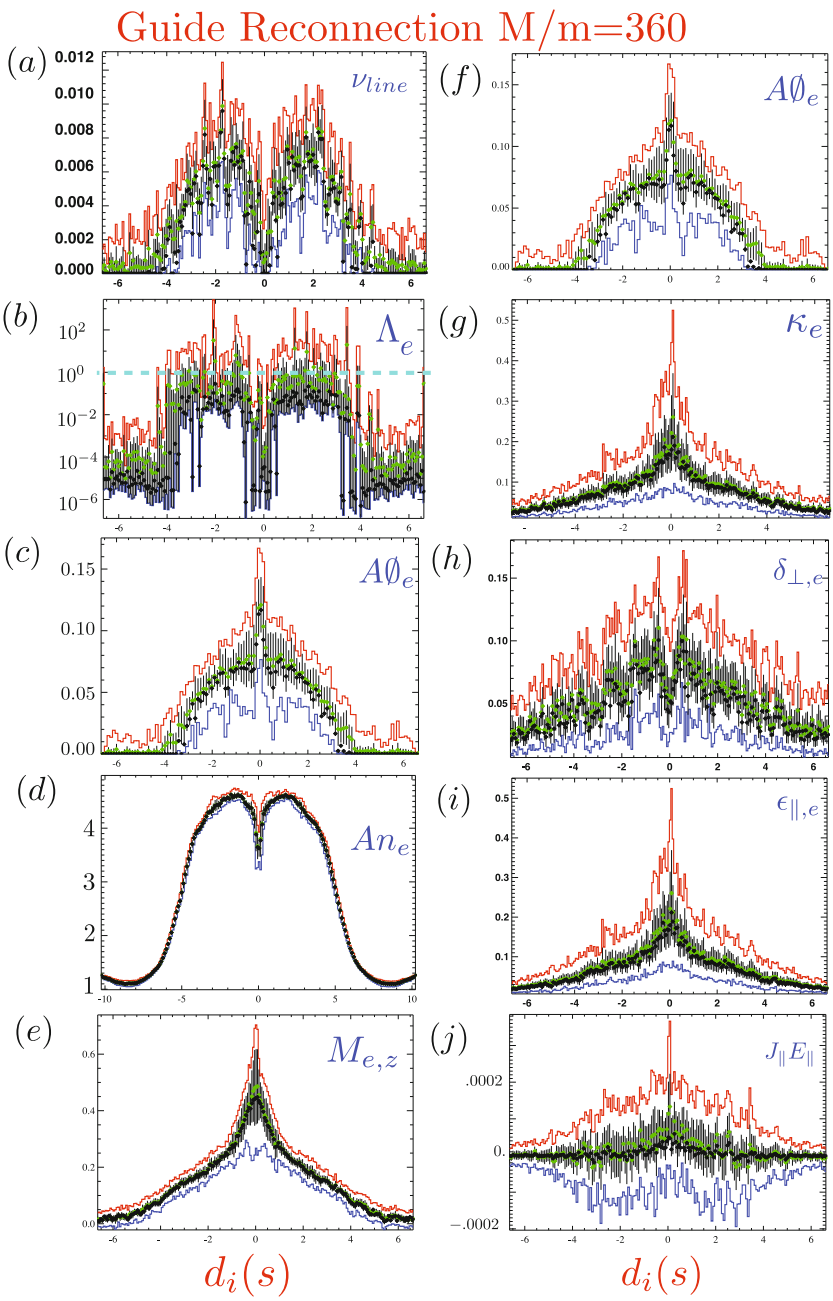

Fig. 2.11 Symmetric Guide $B_z = 0.5B_y$ (Daughton et al. 2006). *Insets* discussed in the text. Colors refer to harmonic (*green*), max(*red*), min(*blue*), variances (*black bar*) about mean (*black dot*) cf. text. Distance d is measured along the center diagonal line in Fig. 2.10c,d, in units. Fig. 2.10d in units of the *local* ion skin depth. *Dashed cyan line* in inset (**b**) is the cross over regime for $\Lambda_e \simeq 1$. *Reproduced with permission from November 2015 Phys. Plasmas, **22**, 101204, Copyright 2015, AIP Publishing LLC* (Scudder et al. 2015a)

below unity along this arm and does not suggest that frozen flux slippage is at the level of a reconnection site. The preferred arm's slippage has a rather pronounced termination at $\pm 4 d_{io}$ along the preferred arm; it also has a significant depression near the center of the arm that is caused by the symmetry of this layer (cf. Scudder et al. 2015a).

A sequence of simulations were done with variable guide field strengths, keeping the interconnection fields the same. While the reconnection rates were observed to be about the same, the level of demagnetization seen at the separator systematically decreased with increasing guide field. In the guide field geometry the conserved reconnection electric field has a strong parallel component, that essentially is an imposition by MHD of $E_{\|}$ much stronger that usual. In addition, the magnetic field has a component along the desired direction of the current channel, giving the current density in the sheet a significant parallel component. In this sense the guide field geometry requires less demagnetization while forming the narrow current channel of the desired intensity, as compared with an anti-parallel geometry. It appears to be the case that less agyrotropy was actually needed to gain access in the solution to the out of plane current needed by the boundary conditions. Nonetheless, Vasyliunas' insight still holds, agyrotropy was still required to support the layer, it was just not as strong as it is in the anti-parallel case. In this sense the anti-parallel geometry while simplest to analyze may be the most complicated as far as gyro orbits. Graphs of these effects are illustrated elsewhere (Scudder et al. 2015a).

2.7.3 2D Guide Asymmetric

Most magnetopause crossings are observed with field strengths and particle densities asymmetric about the current sheet. A fortuitous crossing allowed the EDR to be resolved with the Polar spacecraft that has been diagnosed with the approaches of this chapter (Scudder et al. 2012). Despite the actual 3D geometry of the encounter a 2D asymmetric guide (S = 1) simulation was conducted. It was not possible to achieve the full density asymmetry witnessed in terms of density contrast. A profile through the simulation was found that agreed well with the size and spatial ordering of the observable MacMahon expansion parameters determined from the Polar data that analyzed **E**, **B** and plasma data. The simulation was post processed in terms of the above observable parameters and a pseudo time line was created to move through the spatial mesh of the simulation to gather a possible time series to compare with the spacecraft time series. The fortuitous encounter occurred at very low relative speed (1.6 km/s) and knowledge of this speed and geometrical determinations allowed time intervals to be converted into spatial intervals, providing length scale assignments for event durations. The ordering of the features recorded in the pseudo traverse of the layer in the simulation had many features seen in the data including a large angle shearing of the magnetic field with (different) but electron inertial scale length linear ramps in the magnetic field profile. The profile from the simulation is shown in Fig. 2.12.

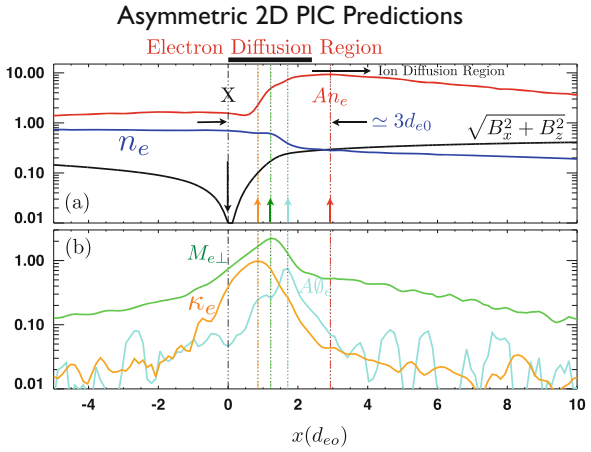

Fig. 2.12 Profiles of in plane magnetic field strength $\sqrt{B_x^2+B_z^2}$, density n_e, and electron anisotropy An_e in panel (**a**) and electron thermal Mach number $M_{e,\perp}$, index of electron demagnetization κ_e and electron agyrotropy $A\emptyset_e$ in panel (**b**) for diagnostic quantities across an asymmetric 2D simulation used for the identification of the resolved EDR in Scudder et al. (2012). Note (in panel **b**) that the $A\emptyset_e$ profile is asymmetrically situated relative to the mach number's indication of the maximum current layer. The anisotropy is on the lower density side of the EDR of the asymmetric layer and its size is anti-correlated with the decrease of $A\emptyset_e$ from its layer peak value. Figure adapted from reference Scudder et al. (2012)

As mentioned before the very low β_e on the magnetospheric side led to an expectation of very high electron pressure anisotropy (> 8), that was recorded by the Polar Hydra instrument, as was significant agyrotropy (> 1) and $M_e > 1.3$. In addition, significant electron heating was found in the reconnection layer. The high anisotropy seen in the simulation was used as an ordering parameter to shuffle the time appearance of the observations as a time series to become a spatially ordered portrait of the layer. This is reproduced in Fig. 2.13, showing the strong quantitative correspondence between the variables observed and expected in the simulation using the reordered data's traverse (Scudder et al. 2012). Particularly extraordinary were the high electron anisotropy$An_e > 7$, *electron* thermal mach number, $M_e > 1.3$, and agyrotropy $A\emptyset_e > 1.2$. These values are previously unheard of extremes for electrons sampled *in situ* in an astrophysical plasma, yet their sizes were corroborated by the PIC simulations. Prominent electron heating is also observed in this crossing, that is clearly different from the thermal state of the plasma on either side of the density transition.

2.7.4 Calibrating Λ_Φ in 2D

Since Λ_Φ is our only thresholded indicator of serious frozen flux violation in 3D, it is important to certify in controlled 2D simulations that the theoretically defined $\Lambda_\Phi > 1$ is properly calibrated so that $\Lambda_\Phi > 1$ and $\Lambda_\Phi < 1$ can be relied upon

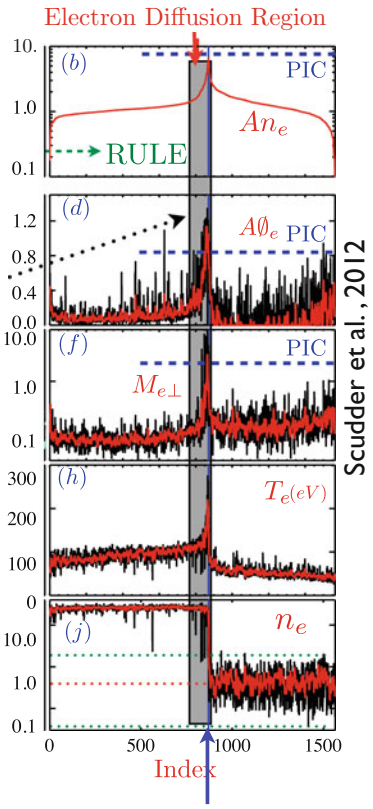

Fig. 2.13 First experimentally resolved electron diffusion region in space plasma that was located between vertical *black line* and vertical *blue line* (Scudder et al. 2012). The *black line* is the experimental location of the separator, the *blue* is the exit into the magnetized inflow region on the magnetospheric sensed by the abrupt decrease of the density indicated in panel (j) (Scudder et al. 2012). Peak PIC suggested values indicated by *dotted horizontal lines* in each panel. Mach number, anisotropy, $A\emptyset_e$, and strong electron heating in panels (f), (b), (d), and (h), respectively of the layer meet or exceed PIC levels expected. Figure adapted from Scudder et al. (2012)

to make the distinction between significant and innocuous frozen flux violations. So far this calibration has been done by comparing with the rates from the flux function, ν_Φ.

A 2D simulation was designed (Scudder et al. 2015a) to assure that our interpretation of Λ_Φ was calibrated, with 1 as the numerical value that signifies "significant frozen flux violation" as at a 2D saddle point which would be called the EDR. A 2D current sheet geometry was initialized with anti-parallel fields perpendicular to the x-y plane that contained all spatial variations; a sinuous, but narrow current interface possessing electron inertial scales separated the two regions of oppositely oriented fields. Had a third direction of variation been allowed this layer would have commenced reconnecting; by the dimensionality of the simulation reconnection was geometrically precluded. For this geometry the spatially varying exhaust arising out of a possible stagnation point would have had to flow along the out of plane (symmetry) direction where no gradients where allowed. The time dependence observed in the simulation was vigorous since the regime was Lower Hybrid Drift unstable. As shown in Fig. 2.14 the subsequent evolution included non-zero frozen flux violations with detectable enhanced variations of Λ_Φ centered on the current ribbon, very large $A\emptyset_e > 1$, and narrow, enhanced $\delta_e \simeq 1$ (not shown),

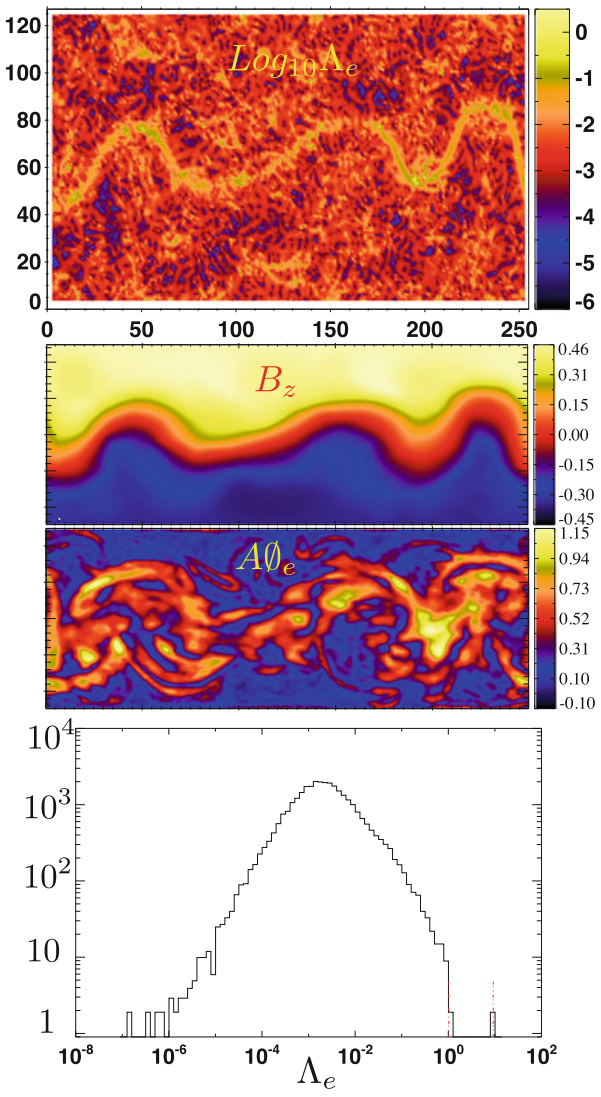

Fig. 2.14 LHDI simulation designed to test Λ_Φ interpretation (Scudder et al. 2015a). 2D simulation conducted in geometry where magnetic reconnection and "significant frozen flux violation" *cannot* occur. The output of the test is what values does the computation of Λ_Φ produce, summarized in histogram form in the *bottom panel*, and spatially in the *uppermost panel*. *Middle panels* show the variation of the component of **B** that would be the interconnecting component if the geometry would allow this process. Spatial variation of $A\emptyset_e$ demonstrates that prominent demagnetization occurs in the narrow channel. But $\Lambda_\Phi \leq 1$ for essentially all grid points, showing that the absence of $\Lambda_\Phi > 1$ is indeed consistent with this simulation where magnetic reconnection is geometrically prohibited. *Reproduced with permission for the November 2015 Phys. Plasmas, 22, 101204* (Scudder et al. 2015a)

confirming the electron inertial scales of the current channels. As shown in the bottom panel of Fig. 2.14 Λ_Φ was generally not zero, but its distribution from all 32,768 cells of the simulation terminated rather precisely at unity; *with only* 0.02 *% of cells indicating mild violations of this threshold*. Of these eight offending cells, only one had an adjacent cell in its eight surrounding cells that also exceeded unity. This lack of reenforcement suggests that this level of violation of the threshold could be viewed as noise in calculating Λ_Φ since the calculation is dependent on the *ratio* of two computed numbers in each cell that involve curls and gradients of curls.

From this test it is concluded that the $\Lambda_\Phi > 1$ threshold is a consistent approach to use when looking for "interesting" locations in 3D simulations, especially given its proofing (cf. Fig. 2.4) to locate saddle points in 2D simulations where reconnection was known to be underway. Below,in Sects. 2.8.1 and 2.8.2, we demonstrate *within* 3D simulations that Λ_Φ and Ψ_Φ are appropriately thresholded.

2.8 3D Reconnection: Exploring Reality

With the loss of the flux function in 3D, Λ_Φ becomes the major model independent tool when looking with computer simulations to identify frozen flux violations. Unfortunately direct measurements in space of Λ_Φ are impractical, even from a suite of spacecraft such as Cluster or Magnetospheric Multi-Scale (MMS). Above we have suggested an observational proxy that may fill this gap. However, for theoretically benchmarking thresholded diagnostics in 3D within PIC simulations Λ_Φ becomes our reference of choice; for the time being it assumes a similar theoretical importance for 3D that the flux function has for 2D modeling.

A recently discussed 3D PIC simulation with guide field equal to the asymptotic reconnection field strength that is asymmetric (Daughton et al. 2014) is used to further study the role of the proposed diagnostics and Λ for finding the interesting layers that could be detected by state of the art spacecraft instrumentation. This simulation was initialized as a Harris sheet and spans the intervals $35d_i \times 85d_i \times 85d_i$ in the x, y, z directions respectively; it used a mass ratio of 100 and was initialized with a profile invariant along the guide (z) field direction. The longer directions of the simulation were along the nominal exhaust (y) and guide field (z) directions with the narrower (x) dimension along the inflow. Higher values of x are initially at weaker density and stronger magnetic fields, providing asymmetric boundary conditions for the current channel formation that is much like what occurs at planetary magnetopauses.

The variation of the current density in the (x-y) inflow-outflow plane (half way along the guide field's z domain) is color coded in Fig. 2.15 at four different times in the evolution. Gross changes to the current density structure occur during this limited time. The superposed yellow contour boundaries were determined for each slice using detailed information in the PIC solution in the form of *tagged tracer electrons* followed during the simulation (Daughton et al. 2011, 2014). The mean value of the tracer tags of all the particles in a cell reflects the dominant origin of the particles, since the tracers from "outside" of the initial Harris sheet carry an immutable tag value of 1 or -1 depending on their initially being on one side or the other of the Harris current sheet. The yellow contours correspond to the mean value of this label being $\mathscr{F}_e = \pm 0.99$, effectively delineating (within the code) the evolution with time of where the "initial electrons on opposite sides" of the current sheet have come to be mixed as enabled by the magnetic reconnection occurring *somewhere* in the simulation, including the possibility that this mixing occurred at some other locale different from the cell possessing this average value. However,

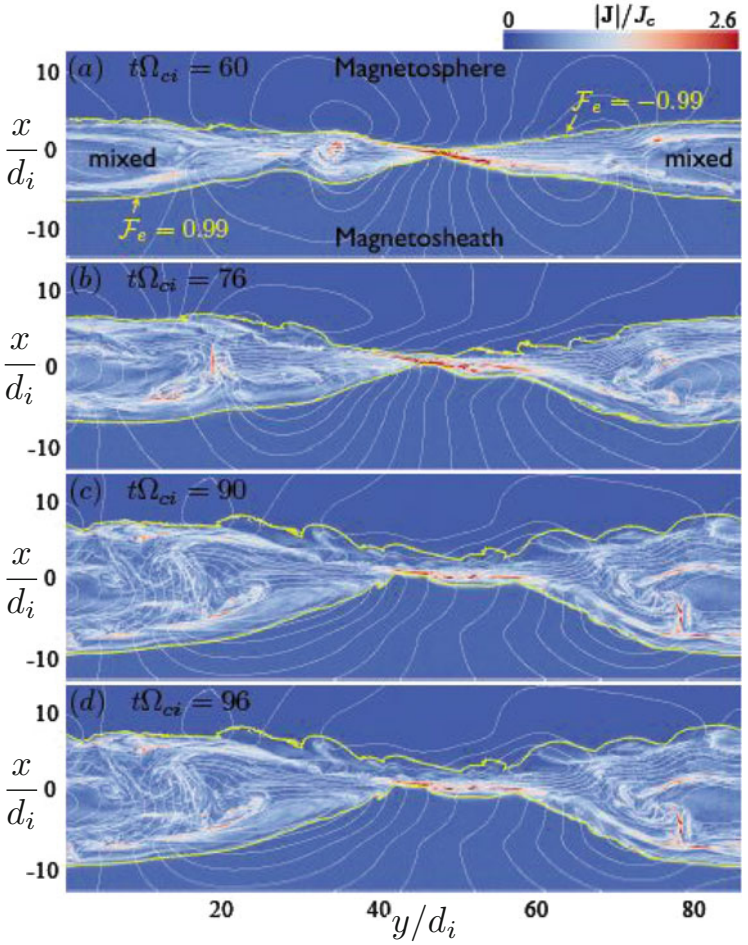

Fig. 2.15 Time evolution of |**J**| from 3D solution viewed in the inflow-outflow plane midway along the guide field direction at four indicated times (Daughton et al. 2014). *Yellow contours* delineate mixing boundaries determined from IC electrons tagged by their spatial positions at t = 0, cf. text discussion. While this boundary is *unobservable*, its determination within PIC does delineate the boundary between unconnected flux regions (*above* and *below* this curve) and interconnected flux tubes between the *yellow curves* where electron mixing is in evidence. In this sense these curves are analogous to the *unobservable* 2D separatrices and should be the boundaries between classes of observables, where interesting *observable* kinetic signatures might be expected. It should be noted that these yellow curves do not necessarily indicate mixing where the curves are seen, but that plasma on either side of these boundaries have been mixed "somewhere" prior to being seen where they are inventoried. *Reproduced with permission from May 2014 Phys. Physics of Plasmas,* ***21****, 052037. Copyright 2014, AIP Publishing LLC*

a mitigating factor is choosing the contour values with absolute value so close to unity, since at 0.99 this represents only a small admixture from the opposite side of the initial current sheet of 1 % of electrons in the cell; this makes such a location near to where mixing is first apparent. The smaller the value of $|\mathscr{F}_e|$ contours, the less direct is the inference of the possibility that such a contour is a site of *local* exchange between the two regimes; conversely small values of $|\mathscr{F}_e|$ indicate more extensive mixing of the initially segregated sides of the Harris current sheet.

Across the four time steps the regions of enhanced current density have evolved and the yellow hour-glass contours have widened perceptively with time, indicative of more integrated electron mobility over its past dynamics. This labeling has been quantitatively used (Daughton et al. 2014) to determine a fast reconnection rate for the simulation, further proofing its capability to differentiate unconnected flux (outside the yellow curves) from interconnected flux inside the hour glass. That calculation gave confidence for using the yellow curves as a separatrix in this 3D geometry, a property deduced in 2D from the flux function alone. Interestingly, in either geometry the separatrices, being topological, are not local observables.

For a given time step one should imagine determining the yellow contours on each 2D x-y plane of the 3D simulation. At the grid resolution the union of all such contours sweep out two surfaces, that crudely look like the two sheets of a hyperbolic cylinder, with its cylindrical axis generally along the guide field direction. The hyperbolic shape is generally correct in each plane along the guide direction, but the surface is more nuanced in the guide direction than found in a formal cylinder swept out by a hyperbolic cylinder of two sheets.

While tagged electrons are certainly *undetectable* in space, their delineation of the yellow "hyperbolic cylinder" in this study with the other results of this simulation can check the reliability of our approach: does $\Lambda_e > 1$ continue to work in 3D as the identifier of where significant frozen flux violations occur, and only inside these yellow boundaries as places? If it does, then finding observable corollaries with $\Lambda_e > 1$ in the code becomes increasingly viable as an observational strategy for identifying 3D reconnection sites in space *without* an *a priori* geometrical template of how it is actually organized (as is provided by the yellow boundaries and tracer tags, which are clearly artificial and not knowable from state of the art spacecraft measurements).

The discretized cylinder $|\mathscr{F}_e| = 0.99$ provides a generalized label for the "inside" versus the outside of the current channel "wedge" of the reconnection pattern. With time the current channel grows, filaments and becomes distorted, even in the plane presented in this picture. There is even evidence that there may be more than one intense current channels, aka "electron diffusion region(s)" present in the system. It is distinctly possible that unlike 2D the union of all sites that are reconnecting may neither be compact, interconnected, or organized in a planar arrangement predetermined by the geometry of the initial conditions. The detection of flux ropes in these 3D simulations (Daughton et al. 2011, 2014) that are forbidden in 2D makes it highly likely that the generalization of *the* EDR in actual 3D circumstances may not be a deformed, but still compact, geometrical version of

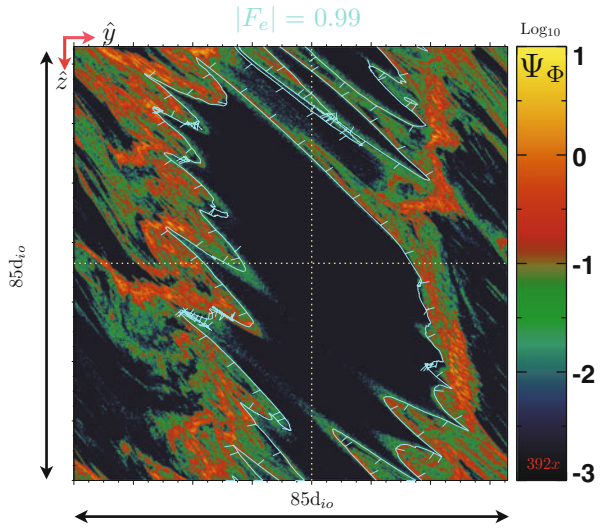

Fig. 2.16 Outflow-guide section of 3-D simulation contrasting *unobservable* level contours of $|\mathscr{F}_e| = 0.99$ (*cyan*) (determined within PIC by following individual macro-particles) with *observable* contours of Ψ_Φ, the proxy for "strong" local violations of frozen flux defined by Λ_Φ (Scudder et al. 2015b). Regions with $|\mathscr{F}_e| < 0.99$ are indicated by the downhill flags on the cyan contours. Consistency is shown in the plane along the guide field direction of Λ_Φ and Ψ_Φ being large only in the regions where $|\mathscr{F}_e| < 0.99$, even when this geometry is rather intricate. See text. From forthcoming paper Scudder et al. (2015b)

the EDR witnessed in 2D, but formed with disconnected sites in its proximity. We will show examples of this below.

2.8.1 Does $\Lambda_\Phi \simeq \Psi_\Phi$ Agree with $\mathscr{F}_e$ Boundaries?

Having traced the mixing of the macro particle electrons within PIC we can contrast the generalized cylinder boundary defined above by $|\mathscr{F}_e| = 0.99$ with the regions of the simulation where $\Lambda_\Phi > 1$ and $\Lambda_\Phi < 1$ which tests the conceptual importance of Λ_Φ for finding locales of different aggregate mixing in the simulation. Since $\Lambda_\Phi \simeq \Psi_\Phi$ the unobservable $|\mathscr{F}_e = 0.99|$ boundaries and the topology of Ψ_Φ are contrasted in Fig. 2.16. An outflow guide (y-z) cut of the simulation results for $\Psi(x_o, y, z)$ are color contoured, with superposed cyan isocontours of $|\mathscr{F}_e| = 0.99$. The plane of this section of the 3-D simulation is $4.4d_{io}$ behind the narrowest thinning of the generalized cylinder. This section of the cylinder defined by $|\mathscr{F}_e| = 0.99$ alternately cuts into the exhausts at either y extreme and is in the inflow regime near the middle of the y domain shown. The wrinkled 3-D nature of the cylindrical surface of mixing defined by $|\mathscr{F}_e| = 0.99$ implies a rather complicated system of cyan contour curves. On each contour the direction "downhill" (towards more mixing) is indicated by the

flags pointing locally perpendicular to the isocontour. Of particular importance is that downhill is the direction to "inside" the 3D wrinkled cylinder; inside according to $|\mathscr{F}_e|$ is the domain of electrons having been (locally or non-locally) mixed from their initial separated states of the Harris initial state of the simulation. Within such a mapped perimeter one should find those possible regions where $\Lambda_\Phi \simeq \Psi_\Phi$ should show up as enhanced. This figure shows that the colored *observable* contours of $Log_{10}\Psi_\Phi > 0$ respect the cyan pattern, with essentially no significant occurrence in the darkest "outside" regions of $|\mathscr{F}_e|$ and all the enhanced values of $\Psi_\Phi \geq 1$ inside the boundary painstakingly defined by following the tags of electron mixing. Further, the colored contours outside (in the inflow) are all weak, i.e. innocuous. It should be also noted that the Ψ_Φ also shows gradations of values with similar shapes as implied by $|\mathscr{F}_e|$ despite the two measures having no direct mathematical contact except through being diagnostics of the single vs aggregates of equations of motion followed by the PIC simulations. Many sections of the 3D simulation have been viewed by the authors in this way, showing the strong reproducibility of the domain of mixing $|\mathscr{F}_e| < 0.99$ (as here) of electrons using the *observable* proxy $\Psi_\Phi > 1$ as a marker for the same condition; conversely, "outside" regions invariably have values of $\Psi_\Phi < 1$. Note that innocuous frozen flux violations also can occur "inside" the mixing cylinder boundary where the frozen flux violations may be strong or innocuous.

2.8.2 Does $\Lambda_\Phi \simeq \Psi_\Phi$ Makes Sense in 3D?

To finish the validation of the concept of Λ we present statistical summaries over the entire 3D simulation frame of the correspondence permitted by comparing with painstaking maps made possible with $|\mathscr{F}_e|$. Using one time slice of the 3D simulation the probability distributions of thresholded frozen flux violations Λ_Φ are illustrated in Fig. 2.17; the red distribution for regions outside the yellow cylinder are more compact in extent than the distribution for the inner region (indicated in black). Using over one billion determinations the red distribution has $P(\Lambda_\Phi) > 1$ only 0.04 % of the time and a most probable value of $0.02 << 1$. The "inside" black distribution of $P(\Lambda_\Phi)$ has a higher mean value although it, too, is still less than unity. However, a significant fraction (1.8 %) of inside cells have $\Lambda_\Phi > 1$. Three points are important here: first, the fraction of outside points with $\Lambda_\Phi > 1$ is very nearly the same as the 0.02 % seen in the 2-D LHDI simulation where reconnection was geometrically prevented. Secondly, $\Lambda_\Phi > 1$ in the inside volume is still rare, occurring with a filling factor of 1:55. Thirdly, Λ_Φ is not a binary indicator, possessing plausible variations and *a continuum of values throughout the simulation* that are typically well below unity; this realization reenforces the need for a finite threshold value (like $\Lambda_\Phi > 1$ for "dynamically interesting frozen flux violations" for use when hunting for the electron diffusion region.

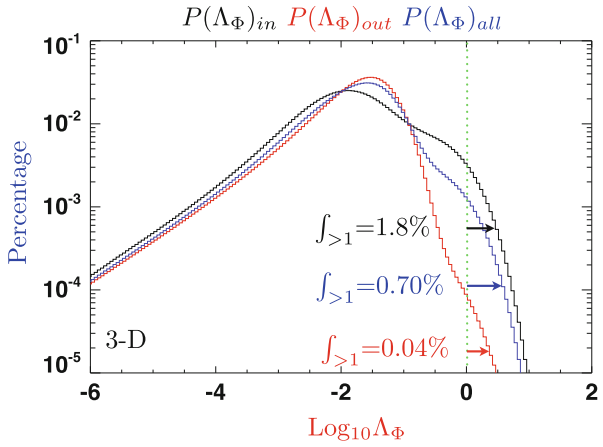

Fig. 2.17 Percentage Probability of occurrence of Λ_Φ segregated by cells outside (*red*), versus inside (*black*), the *yellow* "separatrix" boundaries of Fig. 2.15 (Scudder et al. 2015b). Inventory of the 1.1 billion cells showing the rareness of the condition $\Lambda_\Phi > 1$. A visual presentation of this scarcity in a given plane is presented in Figs. 2.15 and 2.18 below. This figure is from a forthcoming paper Scudder et al. (2015b)

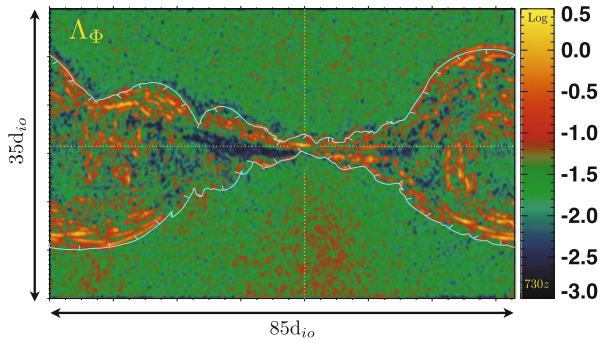

Fig. 2.18 Λ_Φ in section of 3D simulation (inflow-outflow plane) showing regions where $Log_{10}\Lambda_\Phi > 0$; $\Lambda_\Phi > 1$ indicative of a serious level of frozen flux violation as has been witnessed in 2D at saddle points of the flux function (Scudder et al. 2015b). These *bright yellow arcs* are generally in the regions of the hourglass boundaries (*light cyan curve*) of Fig. 2.15 and are candidate layers where reconnection could be identified. This figure is from a forthcoming paper Scudder et al. (2015b)

The inflow-outflow plane's spatial structure for $\Lambda_\Phi(x, y, z_o)$ (Fig. 2.18) illustrates new complexity in the 3-D inflow-outflow plane analogous to that mapped in the 2-D geometry of the bottom inset of Fig. 2.4. Not only are there locations of significant $\Lambda_\Phi > 1$ at the narrowest constriction of the $|\mathscr{F}_e|$ contours, there are many other locales where $\Lambda_\Phi > 1$ in other localized regions both along the separating cyan curves, but also well inside these curves. This contour section was made midway in the simulation volume along the guide axis. This figure also shows

the continuum character of this diagnostic; the "outside" region generally has *non-zero, but innocuous frozen flux slippage levels* with $\Lambda_\Phi < 1$; these regions have longer scales that those at a 2D electron diffusion region, but the scales in the inflow are not infinite, and the curl operation that analyzes the $\mathbf{R}_e(x, y, z)$ sense these finite scales. As in 2D the weak frozen flux violations that occur in these regions are not dynamically important. This is a clear situation where thresholded parameters are required to make decisions.

The inner region of the cylinder shows a higher *mean* value of Λ_Φ for at least two reasons: (1) as a confined region two of its scale lengths are shortened by being spatially confined between the yellow hyperbolas; (2) there are regions within the yellow cylinder (but not outside) where there are "significant frozen flux violations". The probability distribution above shows that in a given plane these violations appear sparse, yet they clearly occur in groupings near the cyan boundary and at places where O points would have occurred in 2D reconnection. [Topological work using this simulation has also identified a separator near the narrowest constriction of the $|\mathscr{F}_e|$ surface and O points inside the expanding wedge of the cylinder (Dorelli, 2014, private communication)]. In addition, there is a new population in the sample comprised of $\Lambda_\Phi > 1$ with values as high a 10–12 with a smooth probability up to those values. Note these regions also include the narrowed down region of the two hyperbolas, that would be the remnant of the initially loaded "separator" line. Statistically this argues that on average as few as 1.8 % of the cells in three dimensional "wedge" region between the yellow cylinder have strong frozen flux slippage. Clearly, there are smaller domains within the wedge where this fraction is significantly higher. Thus the average "filling factor" for $\Lambda_\Phi > 1$ is misleading.

Visually one can see in Fig. 2.18 that the brightest values of $Log\,\Lambda_\Phi > 0$, i.e. $\Lambda_\Phi > 1$, occur within a general hour glass shape, with a large number of order unity arcs found along, but inside, the hour glass shape, although not exclusively. These bright arcs are often in interrupted lanes *in this projection*, but their overarching property is that the frozen flux violation is extraordinarily high in these localized regions. These enhancements are reminiscent of Fig. 2.4 of the 2D guide situation, where enhancements of Λ_Φ are coherent and rising out of the background along (but inside of) the preferred guide separatrices (delineated by the flux function); however, along the mathematical separatrices in 2D we showed that Λ_Φ was still way below unity and strongly contrasted it with the central EDR region where the $\Lambda_\Phi > 1$, the flux function topology displayed the X point geometry, and guiding center parameters were all misordered. However, in 3D this morphology is different with enhancement of Λ_Φ just within the cyan mixing curves as large or higher as occurs at the nominal remnant of the initial Harris sheets separator line seen in this figure.

The lane structure of Λ_Φ *in this plane* is often comprised of curvilinear segments that are often not continuous. It should be kept in mind that any 2D contour presentation is of the signatures apparent in only this plane of the 3D solution. Any three dimensional structures, or curves, that are not parallel to the inflow-outflow plane (of this picture) can appear to start and stop where the otherwise continuous curves pass through the chosen plane for contouring. Further, a ribbon when piercing

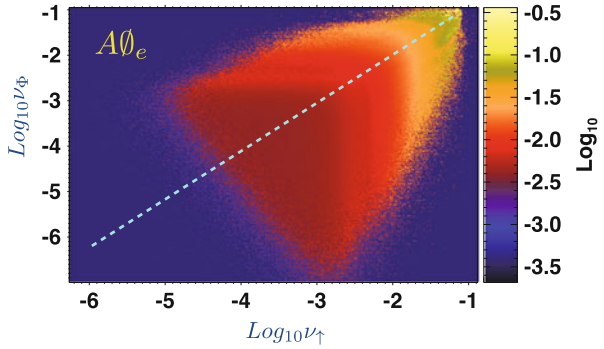

Fig. 2.19 Correlations of the *observable* $A\emptyset_e$ proxy for the *theoretically important, but unobservable* rates of frozen flux: ν_Φ and $\nu_\uparrow$ (Scudder et al. 2015b). Note the wide dynamic rate of frozen flux/line violations across the simulation. Sites of frozen flux/line violation *cannot* be defined in a yes–no binary way. Summary of 1.1 Billion cells in 3D simulation. From forthcoming article Scudder et al. (2015b)

the presentation plane could leave a curvilinear track that reflects more its angle of attack to the presentation plane than its true length. From this vantage point the possible patterns of Λ_Φ when contouring in the plane can have patterns that can generally include dots, line segments and even longer curves depending on this angle of inclination.

2.8.3 $A\emptyset_e$ Organizes ν_j in 3D

In the 2D geometry we have argued that Vasyliunas' insight led to suggesting that the rate of frozen flux violation $\nu_\Phi/\Omega_{ce} \simeq A\emptyset_e$. We argued that this same result remains in 3D, assuming that electron demagnetization is the common enabling concept in 2D and 3D. In this section we show that this relationship is maintained in 3D simulations. Figure 2.19 shows with over 1 billion readings in a 3D histogram that strong $A\emptyset_e$ organizes both strong line $\nu_\uparrow$ and flux ν_Φ violations. The graph illustrates with its color the mean value of $A\emptyset_e$ that occurred in the pixel with coordinates $[\nu_\uparrow, \nu_\Phi]$. Clearly there is general agreement that the rate of frozen flux and line violation increases with increased size of $A\emptyset_e$.

Figure 2.20 uses a two dimensional histogram of occurrence between ν_Φ and Υ to support the expected linear correlation based on arguments above. $[\nu_\Phi, \Omega_{ce}A\emptyset_e]$. For larger values the best fit power law for the suggested relation is 1.1. Given the curls of $\mathbf{R}_e$ involved in ν_Φ vs the local electron pressure tensor eigenvalue calculations for the agyrotropy, this is very good agreement. It should also be noted that ν_Φ is not an observable with the present state of the art space measurements, while the vertical axis involving $A\emptyset_e$ and Ω_{ce} is an observable

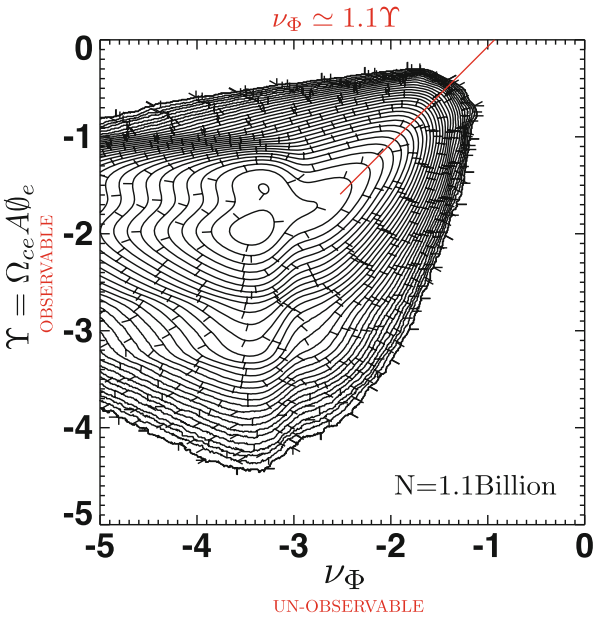

Fig. 2.20 Inventory from 1.1 billion pixels in 3D PIC showing $\nu_\Phi \sim A\emptyset_e$ as a correlation between an "unobservable" ∼ "proxy" appears reasonable, especially when the signals are strongest (Scudder et al. 2015b). *Red* segment shows correlation when signals are strong. From forthcoming article Scudder et al. (2015b)

We suggest that the variable combination Υ:

$$\Upsilon = \Omega_{ce} A\emptyset_e \simeq \nu_\Phi \tag{2.45}$$

produces an observable proxy for the theoretically important, but unobservable *unscaled* rate of frozen flux violation, ν_Φ. Figure 2.21 visually makes this point in two panels, with the top one from the 3D PIC variables giving a direct spatial portrait of $\nu_\Phi(x, y)$, while the bottom panel shows the suggested proxy using other PIC variables that are presently within the state of the art from space observations (such as on MMS). Close replication of details and structures are seen in observable proxy Υ that are seen in the theoretically more direct map from $\nu_\Phi(x, y)$.

2.8.4 $A\emptyset_e \propto \delta^{1\leftrightarrow 2}$ in 3D

While MacMahon suggested that the irreducibly tensorial parts of **P** should scale like δ^2, for weak δ, Fig. 2.22 shows (on either sides of the peak probability) suggestions of two red power laws, scaling as δ_e^2 for frequent, but smaller than peak amplitudes, to δ_e^1 scaling at higher than peak values. A similar trend is also seen in a large collection of estimates from data (Rodriguez et al. 2008; Lopez 2015) Thus the scaling reported in Fig. 2.20 of $\nu_\phi \propto \Upsilon_e^{1.1} \simeq A\emptyset_e^{1.1}$, at the largest values of ν_Φ takes precedence over the small amplitude expectation that $\nu_\Phi \propto \delta_e^2$.

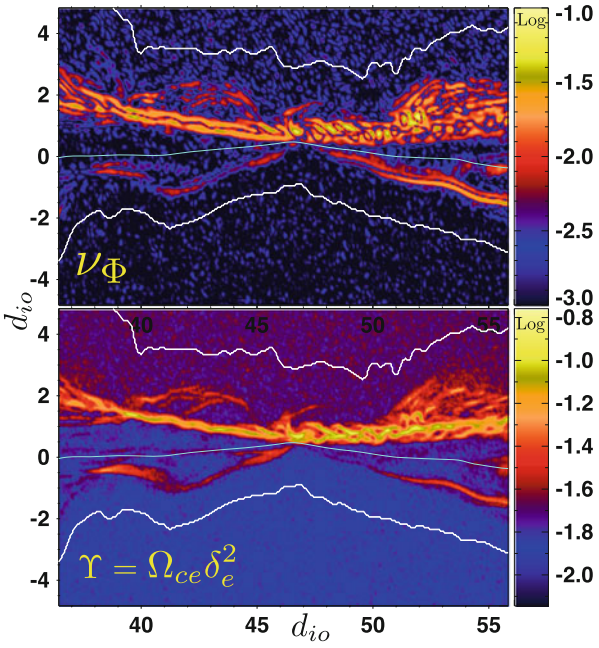

Fig. 2.21 *Top* Close up 2D section near separator of 3D simulation using ν_Φ determined from the $\nabla \times \mathbf{R}_e$ versus *Bottom* the Υ proxy for ν_Φ that is presently routinely observable; from forthcoming paper Scudder et al. (2015b)

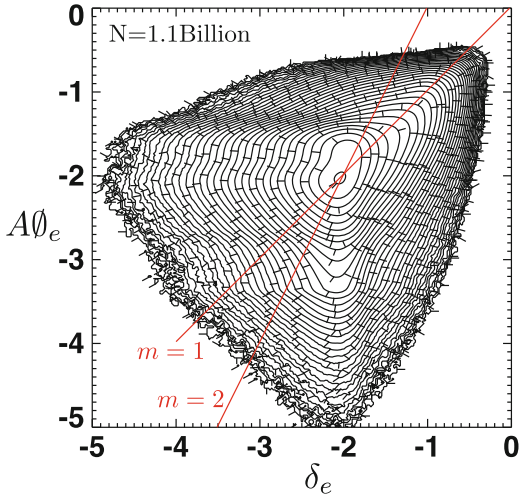

Fig. 2.22 Log–Log correlation of $A\emptyset_e$ scaling with δ_e makes transition from quadratic to linear dependence as δ_e increases (Scudder et al. 2015b). *Red lines* are power laws of index 2 and 1 through the peak of the occurrence distribution. Near and just below the occurrence peak the organization favors quadratic dependence as suggested by MacMahon, but for larger values than at the peak a clear break occurs toward $A\emptyset_e \simeq \delta_e$. From forthcoming paper Scudder et al. (2015b)

2.9 Reconnection Layers in 3D

The variation of the intensity within the 3D PIC solution where $0.001 < \Lambda_\Phi < 3$ is shown by the color contours in three orthogonal isometric sections in Fig. 2.23, with insets a–c corresponding to inflow-outflow, guide-outflow and guide-inflow sections, respectively. The sections are made along dotted lines indicated in their

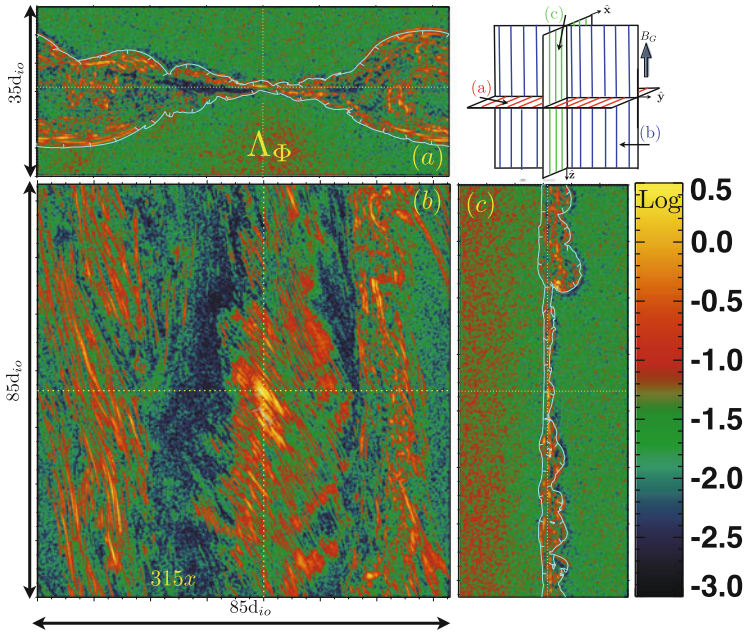

Fig. 2.23 3D Isometric, orthogonal sections of $Log_{10}\Lambda_\Phi$ passing near to the original Harris separator line (x = 315). Geometry of panels (a-c) as extracted from the 3-D simulation cube as indicated in the isometric inset. Note localized enhancement of $\Lambda_\Phi > 1$ shown most clearly in inset (**b**). Also clearly shown is the localization of this region in the guide direction and that the curve of maximum dissipation is inclined to the simulation coordinates. From forthcoming article Scudder et al. (2015b)

orthogonal insets. The contours are color coded according to the common logarithm and the striking variations of color indicate the significant range of variation of this index. Bright yellow regions indicate locales where $\Lambda_\Phi > 1$ and are candidate regions for being reconnection sites. Care should be exercised when interpreting the size of the reconnection layer until three orthogonal projections about a given locale is inventoried. The location of the $|\mathscr{F}_e| = 0.99$ boundaries were pierced by these planes are indicated by light cyan curves. The inset in the upper right hand corner shows the relation of the three sections of the solution shown in the three panels that surround it.

The upper rectangle (inset a) is the inflow-outflow variation as available from a 2D simulation, but here it is literally a horizontal slice of the 3D solution made perpendicular to the guide field direction, color coded by the variation of Λ_Φ. The square panel shows a planar cut that includes the outflow direction on the horizontal and the guide field direction on the vertical. The tall rectangular panel (c) under the inset represents a cross section whose horizontal axis is along the inflow (or thin dimension of the 3D rectangle) and the vertical along the guide field direction. All three sections are isometric sections so that squares in any view contain the same

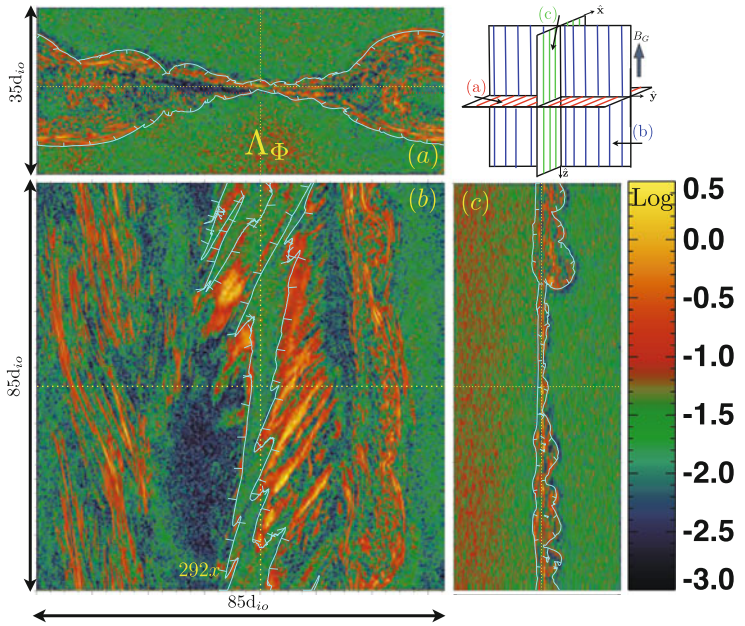

Fig. 2.24 3D Isometric, orthogonal sections of $Log_{10}\Lambda_\Phi$ along cut plane slightly displaced into the high density region, showing the banded enhancements of Λ_Φ on the mixing-separatrix surfaces being cut in both exhausts. Geometry of panels (a-c) as extracted from the 3-D simulation cube as indicated in the isometric inset. From forthcoming article Scudder et al. (2015b)

area. The outflow axes of these cuts is near to the initial separator of the Harris sheet and slightly displaced toward the low density side behind the separator of the Harris sheet.

From these three views we immediately see that the enhanced locations of Λ_Φ are largely near, (1) but inside, the quasi-cylindrical boundary mapped by particle tags indicated here by cyan curves where it cuts the planes of these sections where electrons show evidence of local or non-local mixing (during their prior history) with the outside regime; and (2) occur in a pattern across the rectangular section, with undulations that are organized in a chevron pattern at nearly 45° to the guide field direction. From the side view of the vertical rectangle the high Λ_Φ regions occur all up and down the guide field direction, but the width of the layers of significant frozen flux violation layer that are non-uniform along the guide direction, even showing locales of deep circulation into the low density side.

A 3D section slightly displaced towards the inflow region on the high density side (in front of the Harris separator) is shown in Fig. 2.24, that clearly shows the surface wave type undulations in Λ_Φ that occur generally on the cylindrical boundary determined by $|\mathscr{F}_e|$. Note that the chevron markings are inclined in the opposite direction in this view relative to that previously. The undulations are particularly pronounced on the low density side of the transition (larger x side of cylinder)

where they have been shown to be consistent with LHD waves. The striations in Λ_Φ that follow the ridge wave pattern suggest that large amplitude LHD waves in 3D can induce reconnection in periodic patterns as seen in the yellow regions of enhancements of Λ_Φ. This phenomena cannot happen in 2D simulations and may be the cause for spawning flux ropes that have been reported with this 3D simulation (Daughton et al. 2011, 2014).

In both of these 3D sectional views it is clear that many disjoint sites where reconnection is taking place must be considered. No simple model for the occurrence of the strong frozen flux sites can be anticipated with this level of dynamical freedom. Well inside the cylindrical mixing surface, there is evidence of multiple strands of strong frozen flux violations largely parallel to the guide field direction, but showing evidence of weak helical twists. These layers are in the general areas associated with the O lines identified previously (Dorelli, 2014, private communication).

Even within these exceptional sites of frozen flux violation, there are intensity variations of nearly an order of magnitude. These sections also reflect strands of high Λ_Φ that are rather narrow, but organized obliquely to the plane of these sections. Some evidence for this type of structuring can be seen in the chevron pattern in the square inset (b) of this figure.

A careful inspection of this figure reveals the significant number of sites where $\Lambda_\Phi > 1$ occur; these sites are clearly not localized at the initial separator of the initial conditions, although there is a clear spine of $\Lambda_\Phi > 1$ running down panel (b) that mimics the current patterns and is in the region identified with a separator in this solution (Dorelli, 2014, private communication).

2.9.1 3D Geometry of the Sites of Strong Frozen Flux Violation: Multiple Disjoint EDRs

In this section we examine the locales where $\Lambda_\Phi(\mathbf{X}) > 1$ occur in the simulation, using this scalar as a measure of the intensity of the serious frozen flux violation. It has proven useful to compute the polar angles Θ, Φ about a central point $\mathbf{X}_o$ of the code which we determine as the average of all pixels where $\Lambda_\Phi > 2$. We have chosen to divide the millions of these locales into four groups based on their minimum value of Λ_Φ successively exceeding $j = \{1, 2, 3, 4\}$ Fig. 2.25 depicts the location of the polar angles Φ_j, Θ_j painted with a color reflective of its j value, that in order are (1) gray, (2) cyan, (3) green and (4) red. These locales are painted onto the graph in numerical order so that the nesting of successively stronger regions can be seen. Together they give an overall impression of the ordered geometrical distribution of the sites of very strong frozen flux violations. The branch cut of the Φ_j is at 180°, so that in this coordinate system the nominal outflow jets have $\Phi_{exhaust} \sim \pm 90°$, while the inflow axes are along $\Phi_{inflow} \sim 0, 180 - \epsilon, -180 + \epsilon$, as angles measures in the x-y plane. Θ is the standard polar latitude angle from the $\hat{\mathbf{z}}$ direction of the code which is along the guide field direction.

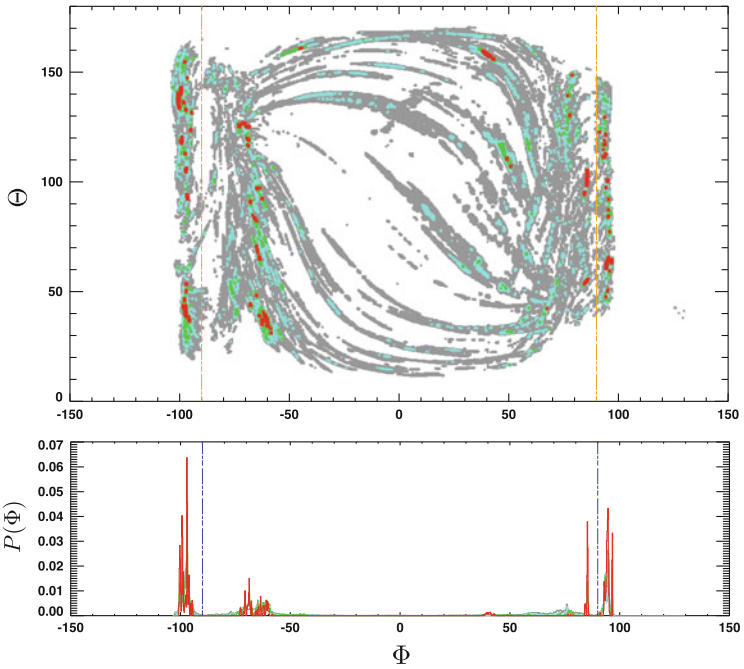

Fig. 2.25 *Top* Loci of polar angles of pixels (about center of pattern) where $\Lambda_\Phi > 1$ *grey*; > 2 *cyan*; > 3 *green*; > 4 *red*. Note predominance of strong signatures in four bands at nearly constant Φ values on either side of $\Phi = \pm 90°$ indicated by *vertical orange lines*. *Bottom* The identification of these four nearly straight *ridges* is facilitated by the probability distributions in Φ constructed by ignoring the Θ values of the pixels in the *top panel*. These ridges correspond to the inner and outer edges of the mixing regions that bound the general exhaust for the central reconnection layer. From forthcoming article Scudder et al. (2015b)

This figure shows that $\Lambda_\Phi > 1$ sites are highly structured in their polar angle locales. Even the weakest signatures (painted in grey) give evidence for lanes of enhanced frozen flux violation with rather intricate patterns. There are two classes of these structures: (i) those that occur with high probability in regions of approximately constant Φ about $\Phi = \pm 90°$, that correspond nicely with the flaring boundaries of the "mixing" boundaries used above to delineate inside and out of the current layer and (ii) a second group of traces/lanes that reach *between* the two disjoint areas of class (i). The lanes of class (ii) appear to radiate from and converge on "poles" with Φ_*, Θ_* coordinates of $(-70°, 125°)$ and $(75°, 50°)$. As the threshold get larger the regions become more compact, but the regions of highest Λ_Φ are increasingly concentrated in four layers of nearly constant Λ_Φ that correspond to half planes from $\mathbf{X}_o$ corresponding to the approximate asymptotes of the mixing boundaries seen in yellow curves in Fig. 2.15 The probability of occurrence of each group with phase angle Φ_j is shown in the bottom panel of this figure. The strongest $\Lambda_\Phi > 4$ grouping gives the sharpest probability profile that is nevertheless consistent with the probability constructed with a lower thresholds.

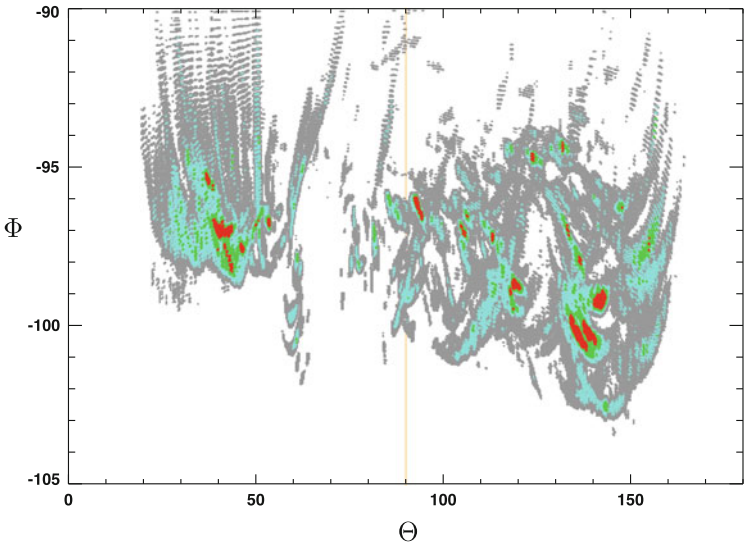

Fig. 2.26 Expanded view of contributions in narrow region of $\Phi < -100°$ for one mixing edge on the high density side of the layer to the *left of center*, showing the striations of occurrence as widely dispersed in Θ but very narrow in Φ. Ray patterns in *grey* suggest undulations/waves causing migration *above* and *below* $\Lambda_\Phi = 1$ thresholds. Rays appear to converge in angle to regions where $\Lambda_\Phi > 4$. There are clearly a large number of disjoint hot spots, *identified as candidate analogues of the EDR in 3D*. From forthcoming article Scudder et al. (2015b)

By focusing ones attention on one of these indicated azimuthal planes where there is high occurrence probability further insight can be achieved of the geometrical distribution of these large Λ_Φ sites. If $\Phi = \Phi_* \sim -100°$, then the selected points can be vernierly segregated in Φ in the vicinity of $-100°$ to show the angular structure and strands that will be suppressed below when trying to inventory the spatial distribution of these regions. Figure 2.26 depicts a high resolution slice of the $\Phi(\Theta)$ distribution found in the near vicinity of the $< \Phi < -100°$ region. This picture gives evidence for structures entering and leaving the region of $\Phi = -100°$ as would be expected with the curved mixing boundary shown above.

Given the thresholding used to make this picture one can see clearly periodic disturbances in Φ interrupted by white as would occur with a wave "train" whose Λ_Φ was oscillatory with peak amplitudes near $1 + \Delta$ where Δ is small. These "trains" have spatial widths of a few degrees in Θ, but can extend $10 - 20°$ in Φ before becoming lost in other signatures of a slightly different orientation.

Curiously, many of these "trains" appear to converge on even stronger Λ_Φ regions highlighted in cyan, green and even red. The closer these trains get to the red regions of intense Λ_Φ the less likely are distinct trains to be seen silhouetted on the white background, as if the $\Lambda_\Phi > 4$ regions were the spatial "source" for these trains? Certainly the most intense regions of $\Lambda_\Phi > 3$ are seen to be disjoint at this resolution. The red zones with $\Lambda > 4$ generally extend a few degrees in either polar

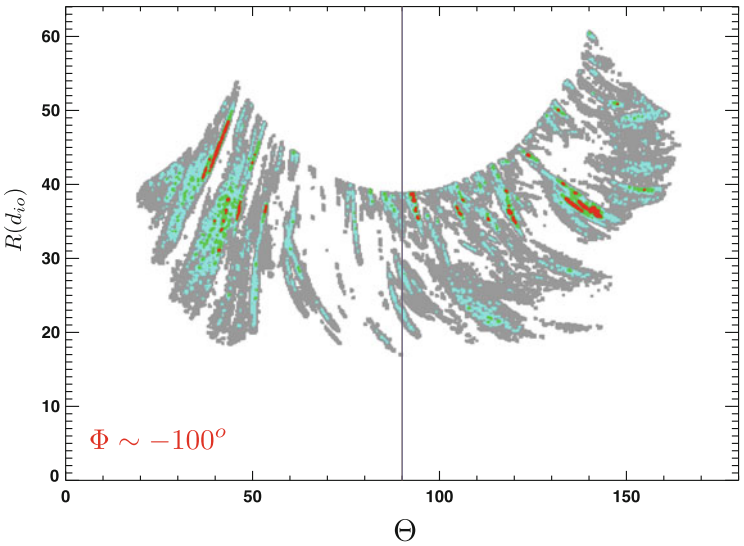

Fig. 2.27 This figure illustrates the latitudinal dependence of the radial distance $R(\Theta)$ for strong violations of frozen flux as color coded by the intensity of Λ_Φ. Multiple ribbons of enhanced violations are shown with typical lengths of $10 - 20d_{io}$. Orderly termination of arcs at maximum radius reflects the variation of the distance to the edge of the simulation box along different Θ values. Strongest violations of frozen flux (*red*) are well removed from simulation boundary. In this plane the location of the Λ_Φ violations range from $20 - 50d_{io}$ from the simulation center. From forthcoming article Scudder et al. (2015b)

angle and tend to be rather compact. In this single half plane there are over 15 such compact very intense frozen flux regions.

Suppressing the $\pm 6^\circ$ spread in Φ in Fig. 2.26 we construct a spatial portrait in Fig. 2.27 of these regions based on the radius, R, and elevation angle, Θ of the pixel. In this figure the horizontal axis is Θ and the vertical axis is the distance R in ion skin depth units from the assumed center of the 3D occurrence of these flux violations. The first impression with this format is that there are many ribbons $R(\Theta, \Phi_*)$ of *reconnection curves*, with lengths of order $5 - 20d_{io}$. In the longer arcs there is usually a $\Lambda_\Phi > 4$ region. The arcs are separated in angle by $> 10^\circ$, which at their distances from $\mathbf{X}_o$ imply spatial separations at times of order $5 - 15d_{io}$ apart.

The upper radial curvilinear boundary to these arcs is caused by the finite simulation box, and serves to show where the strongly enhanced regions of Λ_Φ occur; generally the ribbons and strings enhancements are well away from the simulation's boundary and generally more than $20d_{io}$ away from the center of the simulation rectangle$(35 \times 85 \times 85)d_{io}$. These layers primarily occur along the flaring portion of the "mixing" boundary and correspond to examples of enhanced lanes of $\Lambda_\Phi > 1$ seen in Fig. 2.18 just inside the cyan mixing boundary.

Given our demonstration in this chapter that $\Lambda_\Phi > 1$ is a well calibrated index of the saddle point region in 2D simulations, and correctly predicts LHDI models

are not reconnecting when they are geometrically prohibited to reconnect, and given the agreement between mixed and unmixed plasmas for predicting the incidence of strong frozen flux signatures, it would appear that *there is little room but to suggest that the ribbon like structures with $\Lambda_\Phi > 1$ reported in Figs. 2.25, 2.26, and 2.27 are the analogue in 3D of the EDR of 2D magnetic reconnection.* These structures appear to be present in rather large numbers in restricted regions of the current channel, be $10 - 20 d_{io}$ in length and be concentrated on the mixing boundary that has been previously identified (Daughton et al. 2011).

2.9.2 EDR Closeup

A close up of a strong Λ_Φ region near the narrowest constriction of the mixing boundary is shown in Fig. 2.28. The narrow feature depicted in the projected (a) plane is actually approximately $7 d_{io}$ in length, canted along the guide field direction with an angle similar to those seen in the chevron strips of Λ_Φ shown above. The layer remains thin in cross section in the dimensions transverse to this length. In 3D the signatures of diagnostics in a given plane can look sporadic *in that plane* even though the structures are elongated out of the chosen plane. One has the impression that much of the disjointed curvilinear segments of Λ_Φ seen in plane (a) section

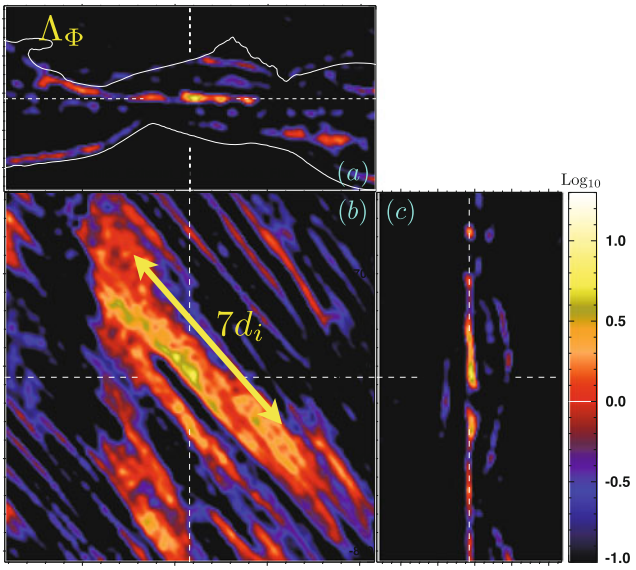

Fig. 2.28 Close up slightly behind separator site of reconnection: orthographic Λ_Φ. Linear dimensions of the square is $11.64 d_{io}$; thin dimension of *top* and *side* sections are $4.79 d_{io}$. Geometry of panels (a–c) as extracted from the 3-D simulation cube as indicated in the isometric inset. From forthcoming article Scudder et al. (2015b)

of the orthographic projections represent such projection effects of structures (as shown immediately above in Fig. 2.25, 2.26, and 2.27) that are smoother when seen in their "natural" geometry where the elongations are in some optimal plane.

2.9.3 *Hints at Local: Global Diagnostics in 3D*

The theoretical underpinnings of magnetic reconnection in 3D involves global properties that clearly challenge an inventory from spacecraft. However, our internal verifications have begun to show some correspondences between what *can* be sampled versus the global quantities that figure in the theory.

One idea is that *quasi-separatrix layers* are the generalization of the separator line which can be defined in 2D reconnection that emanates from the saddle point and is perpendicular to the two dimensional plane where variation is allowed. A property of these layers is that initially close magnetic lines that comprise these layers undergo rapid separation from one another in these locations. The implication is that the cross section of these tubes if they started as circles would become highly elliptical, that is "squashed" in the process (Demoulin et al. 1996; Titov et al. 2002). The measure of this squashing involves integrals (cf. Scudder et al. 2015b; Finn et la. 2014) along field lines over distances comparable to the simulation size, making this assay decidedly non-local and not directly accessible to even a flotilla of spacecraft making current state of the art measurements. In the top panel of Fig. 2.29 values

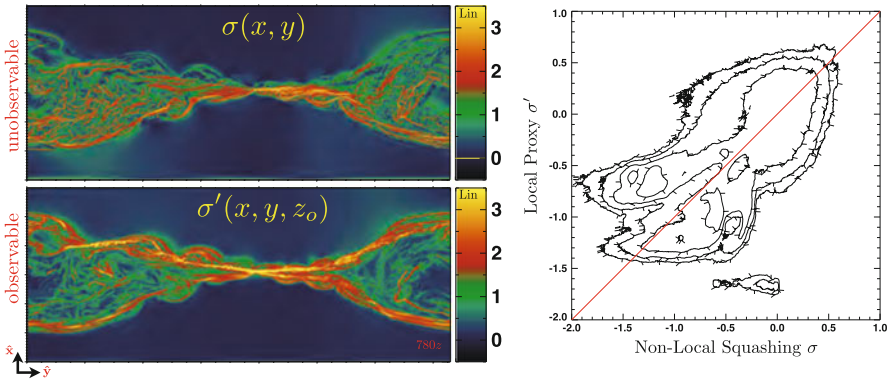

Fig. 2.29 *Top* Global PIC Squashing parameter σ, *Bottom* Local inference of squashing σ' that could be deduced by state of the art spacecraft instrumentation and using a local Harris sheet model to estimate the non-local effects (Private Communication William Daughton, 2015; Scudder et al. 2015b). *Color contours* are shown with linear scales. Some apparent differences on linear scale are present. (*Right*) inset shows the correlations between unobservable global index and local proxy: $[Log_{10}\sigma, Log_{10}\sigma']$, showing their correlation with one another. Note the wide dynamic range of this correlation on Log_{10} graph deemphasizes the color distinctions that appear in the contour comparison using linear scale. From forthcoming article Scudder et al. (2015b)

for the squashing parameter $\sigma(x, y)$ *determined from the full 3D variation of the PIC code* are shown (Daughton, private communication, 2014), while the bottom panel illustrates the proxy value $\sigma'(x, y)$ determined locally using the properties of a *local Harris sheet* model to estimate what value might be expected there. This approach requires use of δ_e summarized above as well as making local determination of normal and guide field geometry along the space track. This figure shows there is a coarse correspondence between the actual line integrals performed within the PIC and local approximations to the squashing factor. The principal assumption of this approach is that the local Harris characterization of the magnetic field at the observer is the dominant determinant of the squashing factor. Other global local connections have been identified (Scudder et al. 2015b).

2.10 Big Picture About Finding Site(s) of Magnetic Reconnection

Our approach to finding reconnection sites with such elusive properties is a form of using sieves of increasing fineness to find documentable sites where collisionless magnetic reconnection is underway. A measure of the fineness of the sieve is how many unwanted objects pass the sieve including your objective. In Fig. 2.1 many structures pass these sieves that are not reconnection sites, but just structure that pass a mass flux—which a reconnection layer does also. Ideally the electron diffusion region would be identified based on there is "no other interpretation" possible for the data.

We have argued in this chapter that electron demagnetization is sufficiently rare in the domain of sampled astrophysical plasmas, that it should be used as a necessary sieve in such identifications *after* the same sieve on almost all other plasmas has determined negligible levels of demagnetization. We have also argued that another macroscopic sieve would involve detecting electron thermal mach number $M_e \simeq 1$; such mach numbers are totally unknown in space plasmas except as theoretically expected in reconnection. Figure 2.1 shows that there are many objects beyond layers thought to be involved in reconnection that pass the sieve represented by these tests. The status quo approach can be markedly improved with these new electron specific sieves. Figure 2.30 gives an overview of the relationships of these sieves, with the coarser jump conditions of Fig. 2.1 well removed from identifying the EDR and with more surgical sieves involving electron kinetic properties as one gets closer to clear identifications. At present the sieves discussed in this chapter are technically possible and would appear to be an exceedingly attractive way to reap the investments of so many research dollars represented by the Magnetospheric Multiscale Mission which seeks to critique experimentally how collisionless magnetic reconnection "really works" in nature.

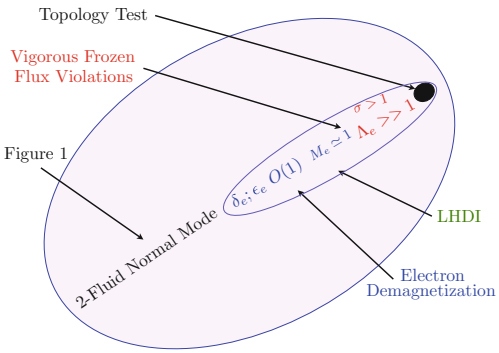

Fig. 2.30 The telescope of scales involved in finding layers certifiably involved in collisionless magnetic reconnection (Scudder 2015). Outside the frame of this figure are 1 fluid jump conditions as summarized in Fig. 2.1 of this chapter. Proximity to the EDR in this figure requires tests of increasing sophistication beyond Hall signatures that are commonplace two fluid features. Careful assays will require electron specific properties certified by the electrons in the plasma. Without evidence to show that the measured thermal electrons are demagnetized, there will be no convincing evidence that the innermost expected current layer of magnetic reconnection has been traversed. From forthcoming article Scudder (2015)

Appendix 1: Role of $R_{ez} \neq 0$ in 2D Flux Slippage

The electric field in terms of the potentials takes the form

$$\mathbf{E} = -\nabla\phi - \frac{1}{c}\frac{\partial \mathbf{A}}{\partial t}. \tag{2.46}$$

For the observer moving with the electrons, the partial derivative becomes an advective derivative and **E** transforms via Galilean relativity while the scalar potential is not modified yielding

$$\frac{d\mathbf{A}}{dt}\Big|_{\mathbf{U}_e} = -c\Big(\mathbf{R}_e + \nabla\phi\Big). \tag{2.47}$$

Since the gradient only has components in the (x-y) plane of the 2D simulation, the total time evolution of A_z is determined by the z component *alone* of the non-ideal electric field:

$$\frac{dA_z}{dt}\Big|_{\mathbf{U}_e} = -c\mathbf{R}_{e,z}. \tag{2.48}$$

Since the components of **B** in the x-y plane set the reconnection topology, and $B_x = \frac{\partial A_z}{\partial y}$ and $B_y = -\frac{\partial A_z}{\partial x}$, the time evolution in 2D of the reconnection topology is controlled only by the non-zero "out of plane component" of the violation of Alfven's "frozen in" condition. While a parallel electric field generally makes

$\mathbf{R}_e \neq 0$, unless $E_\parallel \hat{\mathbf{b}} \cdot \hat{\mathbf{z}} \neq 0$ its violation of Alfvén 's frozen in condition does not affect the slippage of flux in 2D.

A side benefit of the existence of the vector potential is that the isocontours of $A_z(x, y)$ have local normals given by $\mathbf{n} \propto (\frac{\partial A_z}{\partial x}, \frac{\partial A_z}{\partial y})$. Such normals are always perpendicular to the components of $\mathbf{B}$ in the x, y plane, since $\mathbf{n} \cdot \mathbf{B} \equiv 0$ everywhere in the x-y plane. Accordingly contours of A_z provide a simple way for exhibiting the topology of magnetic field lines, without having to integrate the three differential equations for field lines to find out where they go. In 3D the answer to such questions cannot be provided in this way since there is no flux function available.

Appendix 2: The Origin of Two Scales About the Reconnection Site

The mass asymmetry in a hydrogen plasma shows that the electron momentum equation is a natural way to discuss the factors that control the electric field and gives its physics to the Generalized Ohm's law. For those who have learned MHD as a one fluid description of magnetized plasmas, there is a path to seeing that nothing has been lost developing our picture of the current channel with electron myopia. In the so called one fluid picture that underlies MHD the scales of the system are long, the currents are weak, so that it is actually true that $\mathbf{U}_e \simeq \mathbf{U}_i \simeq \mathbf{U}$ where

$$\mathbf{U} \equiv \frac{n_e m \mathbf{U}_e + n_i M \mathbf{U}_i}{n_e m + n_i M} \simeq \mathbf{U}_i. \tag{2.49}$$

In this context Alfvén's ideal approximation shows up in the literature as the assertion that the magnetic fields is displaced by where the Center Of Mass (COM) go, which in this approximation is the same as where the ions or electrons go! This physics is often summarized that the field moves with the ions since they essentially determine the COM. However, as the scales being explored are no longer infinite, gradients and current densities occur and are supported by relative motion between electrons and ions $\mathbf{J} = en_e(\mathbf{U}_i - \mathbf{U}_e)$ and MHD is exported into regions where the density becomes lower and the binary rate ν_{ei} for binary collisions also drops. The plasma still has many other scales regulated by the density and the magnetic field strength that keep the system well organized, especially the gyro scales at right angles to the magnetic field. The time periodicity caused by gyrating about the magnetic field permits certain adiabatic concepts like μ conservation and Guiding Center Drifts to be useful in the description of the medium. The decreased collision rate allows the electrons and ions to become uncoupled thermally, promoting the idea that perhaps it is attractive to forego the single fluid concept because there are no longer thermally exchanging internal energy efficiently by copious collisions. If the ions become demagnetized $\rho_i/L \geq 1$ the currents that they might represent can generate emf's of the Hall variety, that show up in the one fluid's variant of

the Generalized Ohm's Law as $\mathbf{J} \times \mathbf{B}$ forces, that have come to be known as Hall emf's. Hall emf's always occur in the one fluid extended MHD picture when the underlying physics has become two fluid in character.

A similar situation occurs when describing a shock wave: the momentum laden ions hurtle across the shock layer, while the agile electrons do an intricate detour along the shock surface until they cross the shock layer at a different location than the ions did. In a very real way the magnetized electron's agile side step carried the magnetic field along the surface of the shock and delivered it into the magnetosheath some distance from where the demagnetized solar wind ion had pierced the shock. The relatively abrupt, but magnetized motion of the electrons allowed them to label and advect the magnetic field through the shock layer, while the protons, with convected gyro radii thicker than the shock ramp, became demagnetized there, lost there hold on their solar wind field line and propagate downstream in the magnetosheath gyrating about another magnetic field line. Because the ion gyro radius is larger than the electrons, it loses its ability to follow changes in direction of $\mathbf{B}$ more readily than do the electrons. Central to the idea of particles labeling or advecting a field line is that the species can "hold on to", gyrate about, and label the line in question. Clearly ions have more trouble with this than electrons. The earth's bow shock layer is a large amplitude standing whistler wave, a high frequency extension off of the Alfvén wave dispersion branch with wavelengths intermediate between $\rho_e < \lambda < \rho_i$. A whistler is a collective mode (wave) in the magnetized plasma that owes its existence to the distinctly different mobility of the electrons at frequencies approaching the electron cyclotron frequency, which is well above the traditional regime for ideal MHD. It is an example of plasma behavior enabled in the two fluid regime.

However, all is not as nice as it was with large scale one fluid MHD with strong collisions. What happens along field lines with gradients of finite scale? What happens to Alfvén's picture of the magnetic field frozen into the motion of the plasma when the plasma decides to have a split personality with electrons writhing to a different drummer than the ions? There was a degenerate situation for Alfvén's ideal MHD, with three fluid velocities essentially the same because he surmised very weak gradients, very weak current and very low frequencies for such a theory, making the electrodynamics and the mathematics very simple. In fact Alfvén could have announced his frozen flux theorem for ideal MHD by remarking that the electron, or ion or fictional center of mass (COM) fluid carried the magnetic field—since in his postulated regime there was essentially no difference between the three possible fluids. But as the frequencies go up and the scale lengths become *finite* it is no longer true that the preservation of flux is equally true for the observers at rest in the COM frame, the ion frame and the electron. Can the concept of frozen flux persist in the two fluid domain?

The derivation of Eq. (2.6) shows it can be retained until circumstances that cause $\nabla \times \mathbf{R}_e \neq 0$ to occur, at which point the electron flow can no longer presage where magnetic field lines go.

If the same type of derivation were done with the ion momentum equation a similar equation, of equal truthfulness, would be

$$\frac{D\mathbf{B}}{Dt}|_{\mathbf{U}_i} = -c\nabla \times \mathbf{R}_i, \tag{2.50}$$

where the ion's non-ideal electric field is given by

$$\mathbf{R}_i = \frac{\nabla \cdot \mathbf{P}_i + \nabla \cdot (n_i M \mathbf{U}_i \mathbf{U}_i) + \frac{\partial n_i M \mathbf{U}_i}{\partial t}}{en_i}. \tag{2.51}$$

By inspection $\mathbf{R}_i$ can have scales as short as the ion gyro and inertial lengths, ρ_i and d_i. At the shock when the shock layer is thinner than the convected ion inertial length $L = U/\Omega_{ci}$ there will be non-zero contributions from all of these ion terms. Certainly the ion pressure tensor is non-gyrotropic on this scale through the layer, and *Eq. (2.50) correctly indicates that the magnetic flux will no longer be viewed by the ion rest frame observer as being conserved.* At the same place the electrons remain magnetized, its dynamic term is quadratically smaller by M_e^2, and the electron rest observer confidently assays that magnetic flux is being conserved and not slipping in his frame!

While either ion or electron observer's description *of their perception* is technically "correct", the electron observer's description can perceive conservation of magnetic flux down to shorter scales than the ion observer and thus over a wider range of scales of change, essentially because $d_e = d_i/42.84$. Thus the electron observer's decision of frozen flux violation is in some sense the last word because there is no lighter species able to more agilely follow the contortions of **B**. Fortunately, the physicist can pick which frame gives the most information.

A similar situation happens for the plasma as it approaches a reconnection current sheet. Far away from the layer (like electrons and protons in the solar wind way in front of the shock) both species agree the magnetic flux is frozen in their respective frames. However as the plasma approaches the current channel the larger ion gyro radii "feel" the upcoming gradients earlier than the electrons and their $\mathbf{R}_i$ becomes structured with ion gyro scale and inertial scale length structures, that cause the flux to appear to be slipping in the ion frame of reference. Meanwhile the electrons, still well removed in units of *their* inertial scales from the current sheet, experience weak gradients with $\rho_e/L << 1$ so that they remain magnetized and are able to label and advect the magnetic field and deduce that the magnetic flux is essentially frozen in the electron rest frame until coming within several electron gyro radii of the reconnection channel. This is the physical reason for expecting a two zone layer upon approaching the reconnection current sheet.

Confusingly for students this outer layer, where the ions see the magnetic field as slipping with respect to U_i, is referred to as the *ion diffusion region*. The confusion is that according to the electron rest frame observer throughout this outer region, the magnetic field remains totally frozen to the electron bulk motion. None of the mysterious processes that cloud how reconnection happens takes place in this ion

layer, despite some who title papers about this region as about the "diffusion region", leaving the adjective "ion" out of the title. In this sense there is no intrinsic loss of field line identity taking place in this outer, ion layer.

That the ion rest observer makes such a statement says more about his glasses than what is happening! *It is a two fluid regime.* However, this ion inertial layer is a place where ions are making adjustments that electrons are not making. The ions are starting to deflect up and around the obstacle, while the electron are undeterred. This differential response represents a current that implies a $\mathbf{J} \times \mathbf{B}$ Hall electric field is seen by the ion rest frame and COM observers. In this regime pressure gradients of ions and electrons start to form. The electrons remain magnetized as they ExB and diamagnetic drift, and as they do they carry the magnetic field with it, creating the "Hall magnetic patterns" foreseen in theory (Sonnerup 1979) and found in superposed epoch modeling with spacecraft data (Eastwood et al. 2007).

It is only within the electron inertial scaled innermost region of the current channel that the electron rest frame observer detects intense frozen flux slippage; here magnetic reconnection will take place. If anywhere this is the collisionless "diffusion" region. It is increasingly common to see this inner region termed the *electron diffusion region (EDR)*, with the "electron adjective" retained. Although historically in resistive MHD this was a diffusive layer and the solution of a diffusion equation, there is no guarantee from the Generalized Ohm's law that this inner "electron diffusion region" will have profiles that mathematically satisfy parabolic diffusion equations.

This discussion has an experimental corollary relevant for those who would document the behavior of collisionless magnetic reconnection in nature: the phenomenology of the outer ion scale that is called the ion diffusion region is rather common in nature, occurring whenever two fluid behavior is allowed or required. It may be necessary for collisionless reconnection, but the detection of Hall signatures by themselves is exceedingly common. The Hall effects restate that two fluid effects are "in play" in the plasma. In fact, nearly any current system that is identified in space will have such Hall effects attending their occurrence. The behavior of the electrons and ions within shock waves hinge on this differential behavior. The current that flows is caused by the different paths of the ions and electrons as they cross the shock. The out of plane Hall magnetic signature in the reconnection context, is also a well documented feature of the shock layer, representing an out of the coplanarity perturbation (Goodrich and Scudder 1984).

Appendix 3: Traditional Techniques for Measuring Lengths in Space Plasmas

Even the most basic conversion of a time interval Δt on a given spacecraft to a length $|\Delta \mathbf{x}|$ traversed along the normal to the structure,

$$\Delta x = \Delta t \hat{\mathbf{n}} \cdot \mathbf{W}_{rel}, \tag{2.52}$$

involves two unknown *vectors*: $\mathbf{W}_{rel}$, the relative velocity of the s/c sensor to the layer, and $\hat{\mathbf{n}}$, the local normal to the surface whose thickness Δx is desired. (Both vectors are required to be known in a common coordinate system.) Alternately, consider two spacecraft, sampling the "transition" at times t_1 and t_2 separated by a known vectorial distance $\Delta\mathbf{X} = \mathbf{X}(t_1) - \mathbf{X}(t_2)$. By cross correlation the times of the "same" structure may be found t_1, t_2, allowing $\Delta\mathbf{x} = \hat{\mathbf{n}} \cdot \Delta\mathbf{X}$. Such a determination still requires an experimental determination of the surface normal and that the front being encountered is without *spatial* variation direction transverse to the determined normal to the surface; also hidden in this approach is the assumption that the structures are not evolving in time between t_1, t_2 and do not have some wave numbers that support the structure possessing more time independent than others! The final painful fact is that the scales expected are short, with $\rho_e \simeq 1\,km$ at the forward magnetopause. To forestall time evolution between observations, the spacecraft must be rather closely collocated, which they might not be for key signatures that require geometrical characterization. With relative motions of order the Alfvén speed likely, the *time resolution for either of these approaches must be much better than 20 ms* and external knowledge of the surface normal and its local planarity are required to get a well constrained determination. The approaches using Eq. (2.19) offer a much more direct approach for obtaining scale information that only involve scalars.

Acknowledgements This paper summarizes work made possible from a fruitful collaboration over many years with William Daughton, Homa Karimabadi and Vadim Roytershteyn. We gratefully acknowledge NSF Grant No. ATM 1153817, NASA NNX 13AG08G at Iowa, and NASA Heliophysics Theory Program at LANL and SciberQuest. NSF has supported our calculations at Ranger and Kraken and NASA has supported this work through the High-End Computing (HEC) Program through the NASA Advanced Supercomputing (NAS) Division at Ames Research Center. We thank Walter Gonzalez for organizing the symposium celebrating Eugene Parker's contributions to the Physics of Magnetic Reconnection, held at São José dos Campos, Brazil, in March 2014. We also celebrate Gene Parker's contributions in many other areas including mentoring D.A. Tidman as a post-doc who became one of our thesis advisors and Gene's collegial interactions during his long career with our other teachers: B. Coppi, S. Olbert, L. Burlaga and D. Papadopoulis. Editorial comments from SED and computer support from R. Holdaway at University of Iowa are also acknowledged.

References

N. Aunai, M. Hesse, M. Kuznetsova, Phys. Plasma **20** (2013). doi:10.1063/1.4820953
J. Birn, E. Priest, *Reconnection of Magnetic Fields* (Cambridge University Press, Cambridge, 2000)
S.I. Braginskii, *Advance of Plasma Physics*, vol. I (Academic, New York, 1965), pp. 1–97
L.F. Burlaga, *Interplanetary Magnetohydrodynamics* (Oxford University Press, New York, 1995)
L.F. Burlaga, J.L. Lemaire, J. Geophys. Res. **83**, 5157 (1978)
W. Daughton, J. Scudder, H. Karimabadi, Phys. Plasma **13**, 072101 (2006)
W. Daughton, V. Roytershteyn, H. Karimabadi, L. Yin, B.J. Albright, B. Bergen, K.J. Bowers, Nat. Phys. **7**, 539D (2011)

W. Daughton, T.K.M. Nakamura, H. Karimabadi, V. Roytershteyn, B. Loring, Phys. Plasma **21**, 052307 (2014)
P. Demoulin, J.C. Henoux, E.R. Priest, C.H. Mandrini, Astrophysics **308**, 643 (1996)
M.W. Dunlop, A. Balogh, Ann. Geophys. **23**, 901 (2005)
J.P. Eastwood, T.-D. Phan, F.S. Mozer, M.A. Shay, M. Fujimoto, A. Retino, M. Hesse, A. Balough, E.A. Lucek, I. Dandouras, J. Geophys. Res. **112**, A06235 (2007)
J. Egedal, W. Daughton, A. Le, Nat. Phys. **8**, 321–324 (2012). doi:10.1038/nphys2249
J.M. Finn, Z. Billey, W. Daughton, E. Zweibel, Plasma Phys. Controlled Fusion **56**, 064013 (2014)
C.C. Goodrich, J.D. Scudder, J. Geophys. Res. **89**, 6654 (1984)
R.D. Hazeltine, F. Waelbroeck, *The Framework of Plasma Physics* (Perseus, Reading, MA, 1999)
M. Hesse, K. Schindler, J. Birn, M. Kuznetsova, Phys. Plasmas **6**, 1781 (1999); P. Pritchett, J. Geophys. Res. **106**, 3783 (2001); M. Hesse, M. Kuznetsova, J. Birn, Phys. Plasmas **11**, 5387 (2004); P. Ricci, J.U. Brackbill, W. Daughton, G. Lapenta, Phys. Plasmas **11**, 4102 (2004); W. Daughton, J.D. Scudder, H. Karimabadi, Phys. Plasmas **13**, 072101 (2006); L. Yin, W. Daughton, H. Karimabadi, B.J. Albright, K.J. Bowers, J. Margulies, Phys. Rev. Lett. **101**, 125001 (2008)
M. Hesse, T. Forbes, J. Birn, Astrophys. J. **631**, 1227H (2005)
H. Karimabadi, W. Daughton, J.D. Scudder, Geophys. Res. Lett. **34**, L13104 (2007)
A. Le, J. Egedal, W. Daughton, W. Fox, N. Katz, Phys. Rev. Lett. **102**, 85001 (2009)
J.Y. Lopez, Ph.D. Thesis, University of Iowa, 2015
A. MacMahon, Phys. Fluids **8**(10), 1840 (1965)
F.S. Mozer, J. Geophys. Res. **110**, A12 (2005)
T.G. Northrop, *Adiabatic Motion of Charged Particles* (Wiley, New York, 1963)
E.N. Parker, Phys. Rev. **107**, 924 (1957)
G. Paschmann, P.W. Daley, *Analysis Methods for Multi-Spacecraft Data*, ISSI, **SR-001** (1998)
E. Priest, Chapter 3 in *Magnetic Reconnection: Concepts and Applications*, ed. by W.D. Gonzalez, E.N. Parker (Springer, Berlin, 2016)
E. Priest, T. Forbes, *Magnetic Reconnection* (Cambridge University Press, Cambridge, 2000); D. Biskamp, *Magnetic Reconnection in Plasmas* (Cambridge University Press, Cambridge, 2000)
S.L. Rodriguez, J.D. Scudder, F.S. Mozer, C.T. Russell, EOS, 2008AGUFMSM31A1701R (2008)
B. Rossi, S. Olbert, *Introduction to the Physics of Space* (McGraw-Hill, New York, 1970)
K. Schindler, *Physics of Space: Plasma Activity* (Cambridge University Press, Cambridge, 2000)
J.D. Scudder J. Geophys. Res. (2015, in preparation)
J.D. Scudder, W. Daughton, J. Geophys. Res. **113**, A06222 (2008)
J.D. Scudder, A. Mangeney, C. Lacombe, C.C. Harvey, T.L. Aggson, R.R. Anderson, J.T. Gosling, G. Paschmann, C.T. Russell, J. Geophys. Res. **91**, 11019 (1986)
J.D. Scudder, F.S. Mozer, N.C. Maynard, C.T. Russell, J. Geophys. Res. **107**, SMP13-1 (2002)
J.D. Scudder, R.D. Holdaway, R. Glassberg et al., J. Geophys. Res. **113**, A10208 (2008)
J.D. Scudder, R.D. Holdaway, W. Daughton, H. Karimabadi, V. Roytershteyn, C.T. Russell, J.Y. Lopez, Phys. Rev. Lett. **108**, 225005 (2012)
J.D. Scudder, H. Karimabadi, W. Daughton,V. Roytershteyn, Phys. Plasmas **22**(10), 101204 (2015a, in preparation)
J.D. Scudder, W. Daughton, H. Karimabadi, V. Roytershteyn, Phys. Plasmas **22**(10), 101204 (2015b, submitted)
B.U.O. Sonnerup, *Solar System Plasma Processes*, vol. 3, ed. by L.J. Lanzerotti, C.F. Kennel, E.N. Parker (North-Holland, Washington, DC, 1979), p. 45
South West Research Institute, 10160.17-BADCO-01, B.A.D.C.O. for MMS Mission, 5 (2010)
X. Tang, C. Cattell, J. Dombeck, L. Dai, L. Wilson, A. Breneman, A. Hupbach, THEMIS observations of the magnetopause electron diffusion region: large amplitude waves and heated electrons. Geophys. Res. Lett. **40**(12), 2884–2890 (2013)
V.S. Titov, G. Hornig, P. Demoulin, J. Geophys. Res. **107**, SH3-1 (2002)
V.M. Vasyliunas, Rev. Geophys. Space Phys. **13**, 303 (1975)

http://www.springer.com/978-3-319-26430-1

Magnetic Reconnection
Concepts and Applications
Gonzalez, W.; Parker, E. (Eds.)
2016, XII, 542 p. 201 illus., 128 illus. in color.,
Hardcover
ISBN: 978-3-319-26430-1